Abnormal grain growth of
Goss grains in Fe−3%Si steel

3%규소강판 내 고스 입자의 비정상 입자 성장

2020 년 8 월

서울대학교 대학원

재료공학부

김 태 영

Abnormal grain growth of Goss grains in Fe−3%Si steel

지도 교수 황 농 문

이 논문을 공학박사 학위논문으로 제출함
2020 년 7 월

서울대학교 대학원
재료공학부
김 태 영

김태영의 공학박사 학위논문을 인준함
2020 년 7 월

위 원 장 _____ 권 동 일 _____ (인)

부위원장 _____ 한 흥 남 _____ (인)

위   원 _____ 한 찬 희 _____ (인)

위   원 _____ 심 형 석 _____ (인)

위   원 _____ 황 농 문 _____ (인)

Abstract

Abnormal grain growth of Goss grains in Fe-3%Si steel

Tae-Young Kim

Department of Materials Science and Engineering

The Graduate School

Seoul National University

Abnormal grain growth (AGG) or secondary recrystallization, in which certain grains grow significantly larger than other matrix grains, is well known in metallic systems. This phenomenon has been extensively studied in Fe-3%Si steel, where grains of {110}<001> Goss orientation undergo AGG selectively, resulting in a strong Goss texture. The mechanism of the selective AGG of Goss grains has not been clearly understood yet since Goss reported this phenomenon in 1935. The sub-boundary enhanced solid-state wetting (SSW) mechanism, where sub-boundaries increase the probability to grow by wetting and thereby induce AGG in metals. In this paper, based on this mechanism, AGG of Goss grains in Fe-3%Si steel was studied.

At the first, the effect of indentation using hardness testers on abnormal grain growth (AGG) of non-Goss grains were studied in Fe-3%Si steel. The primary recrystallized specimen was locally deformed by indentation under various loads and then heated to

860°C and held for 10 min for recrystallization or recovery. Analyses by synchrotron X-ray microdiffraction (XMD) show that all abnormally-growing grains had sub-boundaries with the misorientation angles below 0.6° whereas no matrix grain had sub-boundaries.

According to this SSW mechanism, the probability of wetting increases with decreasing angle of sub-boundaries, small sub-boundary angles are expected to produce larger abnormal grains than large sub-boundary angles. The effect of sub-boundary angle magnitude on the AGG behavior was studied. All abnormally growing Goss grains had sub-boundaries with misorientations less than 1° and all matrix grains examined had no sub-boundaries. Also, small Goss grains tended to have large sub-boundary angles and vice versa. The results imply that the sub-boundary angle should be a determining parameter of the size of abnormally-growing grains.

Meanwhile, previous difficult experiments, which time sequential observation of abnormally-growing Goss grains in Fe-3%Si steel, was studied by electron backscattering diffraction (EBSD). some matrix grains were isolated at the growth front, which produced island grains. The irregular growth often resulted in incomplete isolation, which produced peninsular grains. Numerous matrix grains were isolated by the impingement of abnormally growing Goss grains. Once matrix grains became isolated, island or peninsular grains, they shrank much faster than before.

On the other hands, penetrating morphologies at the growth front of abnormally-growing Goss grains in Fe-3%Si steel was examined. 102 penetrated grain boundaries and 204 penetrating abnormally-growing Goss grain boundaries were examined. Among the 102 examined penetrated grain boundaries, none of them has low misorientation angles less than 15°, whereas 17.2% of the 204 penetrating grain boundaries have low misorientation angles, and they also have 23.5% of coincidence site lattice (CSL) boundaries. Besides, boundary energies of penetrating Goss grains, which were estimated from misorientation measurements of the three grains in the penetrating morphology, satisfied the energetic condition for SSW along the triple junction line. These results imply that the abnormal grain growth of Goss grains in Fe-3%Si steel occurs by the mechanism of sub-boundary enhanced SSW.

Contents

List of figures

Chapter. 1 Introduction

1.1 Abnormal grain growth in metallic system

Abnormal grain growth (AGG) which is also called discontinuous grain growth or secondary recrystallization has been reported to take place after heat treatment of many cold worked metallic materials [1−10]. During AGG, only a few grains grow exclusively consuming the neighboring matrix grains, which shows a transient bimodal grain size distribution consisting of large abnormally−growing grains and small matrix grains before impingements of abnormally−growing grains. AGG normally occurs when grain growth of matrix grains is inhibited by finely dispersed precipitates or a strong texture [11]. Fe−3%Si steel is the most famous alloy showing AGG. Fe−3%Si steel has been studied more intensively than other systems because AGG in the alloy is unusual in that grains with Goss orientation {110}⟨001⟩ selectively undergo AGG (Fig. 1.1) and as a result a strong Goss texture is evolved after secondary recrystallization. In this alloy, there is a puzzle as to why grains with Goss orientation selectively undergo AGG. Although extensive efforts have been made to understand the puzzling phenomenon since its first discovery by Goss in 1935 [12], the mechanism is not yet clearly understood.

Many suggestions have been made to explain the mechanism of the selective AGG of Goss-oriented grains since 1935. The key question has been why the boundaries of Goss grains migrate much faster than those of other matrix grains. In this point of view, some researchers suggested mechanisms based on the high mobility of boundaries of Goss grains such as coincidence site lattice (CSL) boundary [13-16] or high angle grain boundary with misorientation angle 20-45° [17-20]. However, Etter et al. [21, 22] and Morawiec [23], based on their study on the mobility advantage of grain boundaries of Goss grains in Fe-3%Si steel, reported that the mobility advantage of boundaries of Goss grain is not sufficient to explain the selective AGG of Goss grains. On the other hand, Ushigami et al. [24-26] and Homma et al. [27, 28] reported that Goss grains have a high fraction of $\Sigma 9$ boundaries, which have lower energy than other boundaries. Thereby they can have a benefit to overcome pinning force by precipitates.
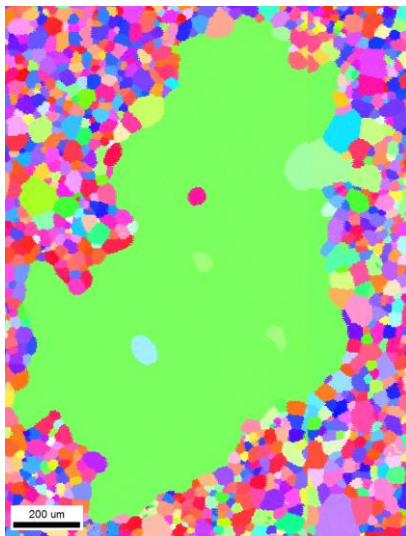
Fig. 1.1. Initial stage of secondary recrystallization of Fe−3%Si steel.

1.2 Sub-boundary enhanced solid-state wetting

Previous theories have limited the cause of AGG phenomenon to grain boundary mobility advantage, however, Hwang et al. [29-32] considered that even if a grain boundary of an abnormally-growing grain has an infinite mobility, it cannot migrate fast enough because of the constraint imposed by the triple junctions. There is a big difference in the growth advantage of a Goss grain between sub-boundary enhanced SSW and other mechanisms. In the former, the growth advantage of a Goss grain come from sub-boundaries in it. Therefore, the primary recrystallization texture of the matrix grains in Fe-3%Si steel is not so critical for AGG of a Goss grain. According to this mechanism, even if some grain has non-Goss orientation, it would grow abnormally if it is made to have sub-boundaries by any means. In the latter, the growth advantage comes from the matrix grains, which should have such favorable orientations that a Goss grain should have a high percentage of high mobility or low energy boundaries when in contact with the matrix grains. Therefore, the primary recrystallization texture is favorable for the exclusive growth of a Goss grain but not so favorable for the other grains.

In fig. 1.2a, if the A grain is to grow towards B grain, no matter how high the C grain boundary mobility, it will be stuck in the triple motion DCE and the FCG and will not be able to move. However, if the triple junction DCE and FCG move towards the B grain, the A

grain may be AGG as shown in fig. 1.2b. As such, the theory of solid-state wetting (SSW) is to explain the cause of AGG phenomenon in the treble function.

However, the triple junction DCE and FCG need to be reasonable in the grain boundary energy γ relationship to move. This means that the relationship

$$\gamma C + \gamma E < \gamma D \tag{1.1}$$

must be satisfied to move towards the triple junction DCE and B grain, and the relationship

$$\gamma C + \gamma G < \gamma F \tag{1.2}$$

must be satisfied to move the triple action FCG towards the B grain. These conditions are wetting condition. If the energies of grains boundaries connected to the triple junction satisfy the wetting condition, the triple junction wetting occurs and triple junction move fast along the triple junction line.

Fig. 1.3 shows the effect of sub-boundary on energy anisotropy and enhancing mechanism. Consider the three grains A, A* and B. If there is a sub-boundary between grain A and grain A*, grain boundary energy γ_{AA*} is very small. So the sum of γ_{AA*} and γ_{A*B} is smaller than γ_{AB}, so the grain A can grows towards grain B. In other words, sub-boundary increases the probability of SSW.

In relation to this mechanism, Park et al. [33] and Shim et al. [34] confirmed experimentally that only Goss abnormal grains had sub-boundaries in Fe-3%Si steel. The exclusive existence of sub-boundaries was also confirmed in the abnormally-growing grains in

5

Al 5052 alloy [35]. In addition, 3-dimensional Monte Carlo (MC) [36-38] and Phase Field Model (PFM) [39] simulations showed that the selective AGG of Goss grains can be satisfactorily explained by sub-boundary enhanced SSW because sub-boundaries drastically increase the probability of wetting along the triple junction line. Meanwhile, Christian et al. [40] suggested that the growth of abnormally-growing grains is highly irregular, producing a fractal shape in the Pd-Au alloy. It should be noted that the highly irregular fractal shaped morphology was reproduced by 3-dimensional MC simulation of AGG by sub-boundary enhanced SSW [41]. Even when sub-boundaries were made in non-Goss matrix grains by indentation in Fe–3%Si steel, indented non-Goss grains grew abnormally [42].
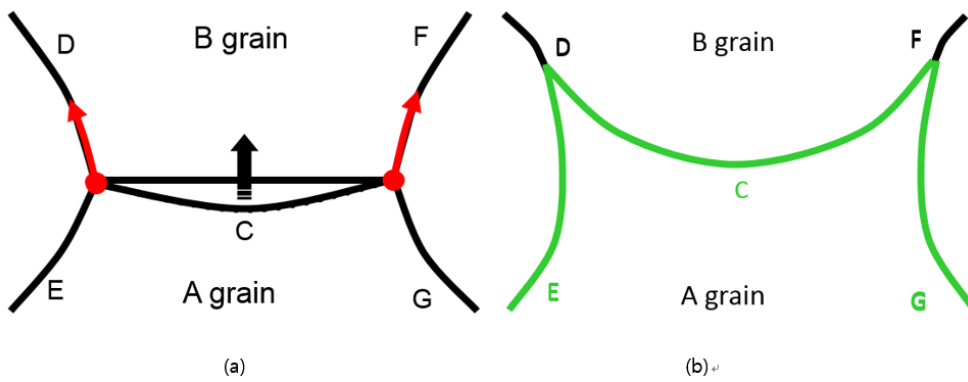
Fig. 1.2. Schematics of solid−state wetting mechanism.
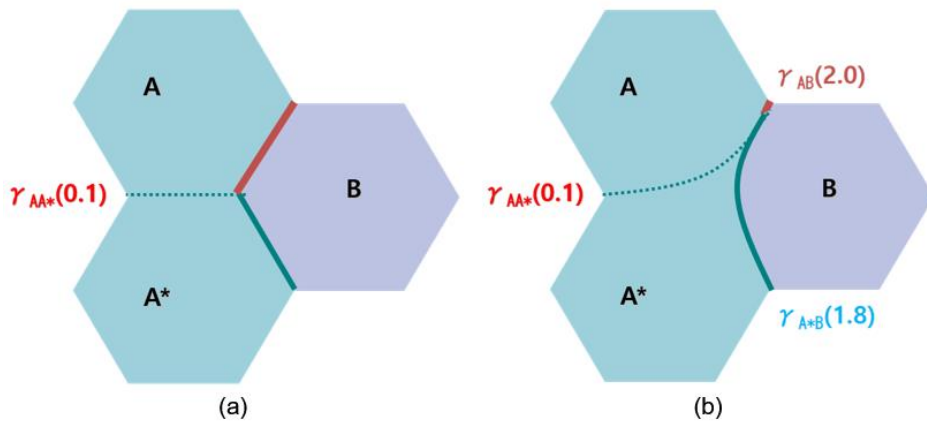
Fig. 1.3. Schematics showing how the sub−boundary of low energy can increase the probability of SSW.

Chapter. 2 Abnormal grain growth of non-Goss grain in Fe-3%Si steel using indentation

2.1 Introduction

As mentioned in Chapter 1, sub-boundaries are the exclusive feature of abnormally-growing Goss grains in Fe-3%Si steel. In other words, sub-boundaries should play an important role in selective AGG of Goss grains in Fe-3%Si steel. If this suggestion that AGG occurs by SSW mechanism and that sub-boundary plays a key role in selective AGG are reasonable, the grains which do not have Goss orientation should undergo AGG during secondary recrystallization as shown Fig. 2.1. Motivated by this background, the purpose of this chapter is to investigate the effect of indentation, which is made by the indenter of a hardness tester, on the AGG of Fe-3%Si steel. Such local deformation by indentation of the primary recrystallized specimen made non-Goss grains undergo AGG during heating. In order to check the existence of sub-boundaries, the specimens were analyzed by synchrotron X-ray microdiffraction (XMD).
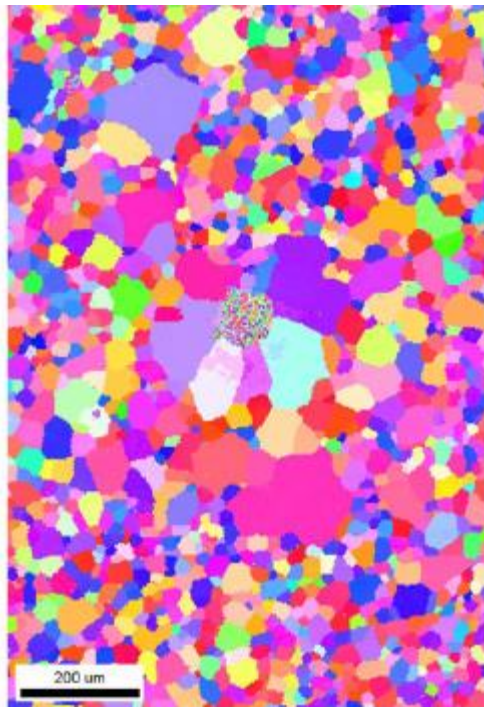
Fig. 2.1. Abnormally-growing non-Goss grains in Fe-3%Si steel.

2.2 Experiments procedure

 A material used in this study was Fe-3%Si steel which contains aluminum nitride (AlN) as a grain growth inhibitor to manufacture the highly grain-oriented electrical steel. An ingot of Fe-3%Si steel was hot rolled to 2.3mm then cold-rolled to 300μm in thickness. In order to produce sub-boundaries, indentations were made on specimens after primary recrystallization, using two types of indenter Micro AIS and AIS 3000 (Frontics Inc). Micro AIS was used for loads of 0.01, 0.05, 0.1, 0.2, 0.5 and 2 kgf with a Vickers indenter and AIS 3000 was used for loads of 3, 6, 12 and 18 kgf with a Brinell indenter. Indented specimens were heated to 860 $^{\circ}$C and held for 10 min for recrystallization or recovery, during which sub-boundaries tended to form by dislocation arrangements around indented areas. Then the specimens were heated to 1080 $^{\circ}$C at 5 $^{\circ}$C /min held 0 s and rapidly transferred from the hot zone to cold zone near the exit of the tube furnace in flowing H_2. This heat treatment was intended to produce a microstructure of the initial stage of AGG. It should be noted that heating to 1080 $^{\circ}$C at 5 $^{\circ}$C/min is a typical condition for Goss grains to undergo AGG. If the heat treatment at 1080 $^{\circ}$C was prolonged or the cooling rate was slow, AGG of Goss grains could occur extensively, which would make it difficult to examine the AGG behavior induced by indentation.

 For specimens indented with loads below 1 kgf, the indentation mark was so small after heat treatment that, after polishing and

11

etching, it tended to disappear or was indistinguishable from non-indented areas by an optical microscope (OM) (Nikon, Eclipse L150). In order to distinguish indented areas of these specimens, these specimens were observed by scanning electron microscope (SEM) (Hitachi, SU-70). Although indented areas could be identified by SEM, individual grains could not be identified by SEM because these specimens were not etched. Therefore, EBSD (EDAX, Hikari) was used to identify whether AGG occurs or not in indented areas. For specimens loaded with 2, 3, 6, 12, and 18 kgf, however, the indentation areas were large enough to be identified by OM after the specimens were polished and etched. Individual grains could be clearly identified by etching with 65% H_2O-35% HCl for 10 s at 100 °C.

To check the possibility that abnormally-growing grains in the indented area might have sub-boundaries, synchrotron white beam (XMD) experiments were conducted on 4B beamline at the Pohang Accelerator Laboratory (PAL) to determine the crystallographic orientations of grains in the microstructure. The sub-boundaries are very small misorientations less than 1° and can be resolved with both the commercial EBSD equipment and synchrotron XMD. However, since the penetration depth of the EBSD electron beam is only ~1 μm, the analysis will be limited to a thin layer of the specimen surface. Therefore, it is difficult to distinguish whether internal misorientations are caused by sub-boundaries or the surface topology. On the other hand, since the penetration depth of

the synchrotron XMD is 10–100 μm, sub–boundaries can be identified without being sensitively affected by the surface topology [43]. This is why the synchrotron XMD instead of EBSD was used to identify sub–boundaries in this study. The PAL has a configuration of Laue diffraction, which provides the information as to the grain orientation. Beam splitting in Laue diffraction patterns indicates the existence of sub–boundaries [44].

The incident white X–ray beam was focused on 1 μm×1 μm using a Kirkpatrick–Baez (K–B) mirror system, and the specimen was mounted on a stage in 45° reflective geometry. Laue diffraction images were collected by a charged coupled device (CCD) X–ray detector (Bruker, APEX II). More details on experimental configuration can be found in the previous paper [45]. The area around the indentation mark was scanned two dimensionally with a step size of 3–9 μm. Laue diffraction images were collected at each step so that approximately maximum 10,000 images per one specimen were used for analysis. To calculate the crystallographic orientation of grains, the geometry of the specimens was calibrated using an unstrained Ge (111) single crystal.

Based on Laue diffraction images, a crystallographic orientation map was obtained through indexing Laue diffraction peaks and calculating crystallographic orientations. And Laue diffraction peaks of all grains in the scanned area were investigated with a focus on the splitting of diffraction peaks, which is known as a typical phenomenon indicating the existence of sub–boundaries inside

grains [44]. Laue diffraction peaks are expressed in the $\chi - \theta$ space where χ is the angle of the diffracted beam within the plane perpendicular to the incident X-ray beam and θ is the Bragg angle. X-ray microdiffraction analysis software (XMAS) [45, 46] was used to index and analyze Laue diffraction peaks, and finally to calculate orientations.

The step size of the EBSD or the synchrotron XMD is determined according to the grain size in such a way that about 10 points of measurements may be included in each grain. Considering the grain size, the step size of the EBSD was 3 μm (Fig. 2.3), and the minimum and maximum step sizes of the synchrotron XMD were respectively 3 μm (Fig. 2.4) and 9 μm (Fig. 2.10). On the other hand, the matrix grain size is in the range of 30-40 μm. Therefore, the step size of 3 μm would be enough to examine the existence of sub-boundaries. It should be noted that when the step size of the synchrotron XMD was 3 μm, the existence of sub-boundaries was not identified in the matrix grains but identified only in the abnormally-growing grains.

2.3 Results

Fig. 2.2 shows the OM images of the polished and chemically etched surface after the specimens of Fe－3%Si steel were heat treated with indentation loads for Fig. 2.2a－2.2d being respectively 3, 6, 12 and 18 kgf. The circular black area at the center of each OM image represents the indentation mark formed by the Brinell indenter. Large grains around the indentation mark, which have a contrast different from matrix grains, are abnormally－growing grains. Fig. 2.2 shows that AGG occurred around the indentation area in all specimens, indicating that the heat treatment after indentation induces AGG. When the indentation loads were 3 and 6 kgf, only one grain appears to have undergone AGG (Fig. 2.2a and b). When the loads were 12 and 18 kgf, however, two or more grains underwent AGG (Fig. 2.2c and 2.2d).

It is known that grains of Goss orientation tend to undergo selective AGG in Fe－3%Si steel [12]. Therefore, one might expect that abnormally－growing grains in Fig. 2.2 would have Goss orientation. Although the OM image in Fig. 2.2 cannot tell whether these abnormally－growing grains have Goss orientation or not, the orientation analysis by synchrotron XMD clearly reveals that they do not have Goss orientation, which will be explained later in detail.

The inverse pole figure (IPF) map represents the orientation of each grain by color, using the EBSD software (EDAX, OIM analysis) and orientation data collected from EBSD or synchrotron

15

measurements. Fig. 2.3 shows the EBSD IPF maps of the specimens after being indented with loads of 0.2 kgf (Fig. 2.3a) and 0.5 kgf (Fig. 2.3b) followed by heat treatment.

In Fig. 2.3, there are many unidentified EBSD points, whose area corresponds to the step size of EBSD. These error points are attributed to not being able to match the related Kikuchi patterns and failing to determine the crystallographic orientation. These errors points are thought to come from the non-flat surface made by indentations. Especially, the area clustered with these error points inside abnormally-growing grains in Fig. 2.3a and 2.3b would correspond to the indentation mark. This means that AGG occurs around the indentation area, indicating that the heat treatment after indentation induces AGG. It should be noted that Vickers indenters were used for loads of 0.2 kgf (Fig. 2.3a) and 0.5 kgf (Fig. 2.3b).

EBSD IPF maps in Fig. 2.3 reveal that abnormally-growing grains do not have Goss orientation but have crystallographic orientations (90.1º, 23.8º, 82º) in Fig. 2.3a and (260.6º, 45.5º, 228.5º) in Fig. 2.3b in terms of Euler angle (φ_1, Φ, φ_2) representation with their misorientation angle with the Goss grain being 49.1º and 45.3º, respectively.

AGG of non-Goss orientation in Fig. 2.3 cannot be explained by conventional mechanisms on selective Goss AGG. One possibility, which was suggested in the mechanism of sub-boundary enhanced SSW, would be that the indentation formed sub-boundaries by the recovery process during heat treatment, which eventually induce

16

AGG. If this scenario is correct, sub-boundaries must exist in abnormally-growing grains in Fig. 2.3. However, misorientation angles made by sub-boundaries are too small to be measured by EBSD. This is why synchrotron XMD was used. Synchrotron XMD, which has extraordinarily high angular resolution [44-47], can not only detect the existence of sub-boundaries but also calculate the crystallographic orientation of grains. It also has an advantage of analyzing a relatively large area in comparison with transmission electron microscopy (TEM).

Figs. 2.4 and 2.5 show the results obtained by synchrotron XMD for specimens indented under loads of 0.2 kgf and 0.5 kgf respectively. Figs. 2.4a and 2.5a show the synchrotron XMD IPF map. It should be noted that the specimens for Fig. 2.3a and 2.3b are identical respectively with those for Figs. 2.4a and 2.5a. Therefore, the orientations of EBSD IPF maps in Fig. 2.3a and 2.3b coincide with those of synchrotron IPF maps respectively in Figs. 2.4a and 2.5a although the magnitude of the scanned area is slightly different between EBSD and synchrotron XMD maps. The coincidences of IPF between Figs. 2.3a and 2.4a and between Figs. 2.3b and 2.5a indicate that the orientation analysis using the synchrotron XMD is reliable.

It should be noted that many unidentified EBSD error points in Fig. 2.3a and 2.3b are absent in Figs. 2.4a and 2.5a. This would come from the difference in the penetration depth of the two beams. The penetration depths of EBSD electron beam and synchrotron X-ray

are respectively ~1 μm and 10–100 μm [34].

It is known that the Laue diffraction beam splits in the area of sub- boundaries and therefore the existence of sub-boundaries is known by beam splitting of Laue diffraction [44]. Considering this, we investigated all Laue diffraction beams in the scanned areas of Figs. 2.4a and 2.5a to check if the splitting occurs. The region where the beam splitting occurs is denoted as 'A' in Figs. 2.4a and 2.5a, which happen to be inside abnormally-growing grains. This result indicates that matrix grains do not have sub-boundaries but only abnormally-growing grains have them.

The splitting in the region 'A' in Figs. 2.4a and 2.5a occurs for and (114) Laue diffraction beams respectively as shown in Figs. 2.4b and 2.5b. Corresponding intensity profiles of the splitting beam in the region of 'A' are shown along the splitting direction ξ respectively in Figs. 2.4c and 2.5c. In other words, the beam splitting in Figs. 2.4b and 2.5b corresponds to the peak splitting in Figs. 2.4c and 2.5c. The misorientation angle of the sub-boundary can be calculated from the distance between two intensity maxima along the splitting direction ξ [46]. From the intensity profiles in Figs. 2.3c and 2.4c, the misorientation angles of sub-boundaries in regions of 'A' in Figs. 2.4a and 2.5a were calculated to be respectively 0.35° and 0.44°.

Such splitting of Laue diffraction beams occurs exclusively in abnormally-growing grains in all specimens indented under loads of 2, 3, 6, 12 and 18 kgf, indicating that AGG might be related with

18

sub-boundaries. Under the indentation loads of 2, 3 and 6 kgf, one abnormally-growing grain was observed around the indented area but two regions in the abnormal grain show the beam splitting as designated as 'A' and 'B' in Figs. 2.6a, 2.7a and 2.8a. The corresponding beam splittings are shown respectively in Figs. 2.6b, 2.7b and 2.8b. The corresponding intensity profiles are shown respectively in Figs. 2.6c, 2.7c and 2.8c. The misorientation angles of the sub-boundaries in regions 'A' and 'B' are respectively 0.31° and 0.22° as shown in Fig. 2.6c, 0.55° and 0.6° in Fig. 2.7c and 0.3° and 0.55° in Fig. 2.8c.

For the indentation loads of 12 and 18 kgf, three and eight grains underwent AGG as shown respectively in Figs. 2.8a and 2.10a. The splitting of Laue diffraction beams was observed at two regions of 'A' and 'B' in the leaf-green abnormal grain, at the region of 'C' in the amethyst-purple abnormal grain and at the region of 'D' in the pansy-purple abnormal grain in Fig. 2.9a. The four corresponding beam splittings and intensity profiles are shown respectively in Fig. 2.9b and 2.9c. The misorientation angles of sub-boundaries in the regions of 'A', 'B', 'C' and 'D' in Fig. 2.9a are respectively 0.35°, 0.23°, 0.4° and 0.4° as shown in Fig. 2.9c.

In the specimens of Fig. 2.10, eight regions of 'A' - 'H' show beam splitting, each of which was located inside eight abnormally-growing grains as shown in Fig. 2.10a. The eight corresponding beam splittings and intensity profiles are shown

respectively in Fig. 2.10b and 2.10c. The misorientation angles of sub−boundaries in the regions of 'A' − 'H' in Fig. 2.10a are respectively 0.28°, 0.3°, 0.37°, 0.43°, 0.38°, 0.2° (0.37°), 0.35° and 0.5° as shown in Fig. 2.10c. It should be noted that the beam in the region 'F' has two splittings as shown in Fig. 2.10b and as a result two misorientation angles as shown in Fig. 2.10c.

In the whole area of the specimen scanned by synchrotron XMD in Figs. 2.4−2.10, there were 2377 matrix grains and 16 abnormally−growing grains. None of Laue diffraction beam splitting was observed in 2377 matrix grains whereas beam splitting was observed in all 16 abnormally−growing grains. In other words, sub−boundaries exist only in 16 abnormally−growing grains. This result indicates that sub−boundaries are a distinctive feature of abnormally−growing grains. The misorientation angle of all 20 sub−boundaries measured here was less than 0.6°.
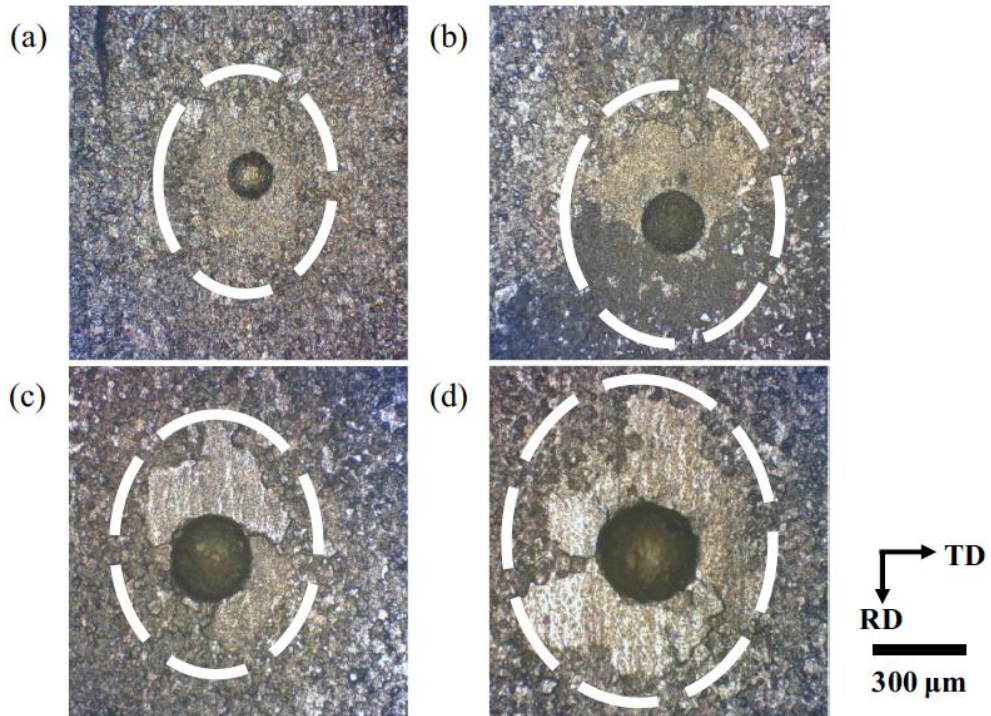
Fig. 2.2. OM images of the specimens polished and etched after indentation and heat treatment. The indentation loads were (a) 3 kgf, (b) 6 kgf, (c) 12 kgf and (d) 18 kgf.
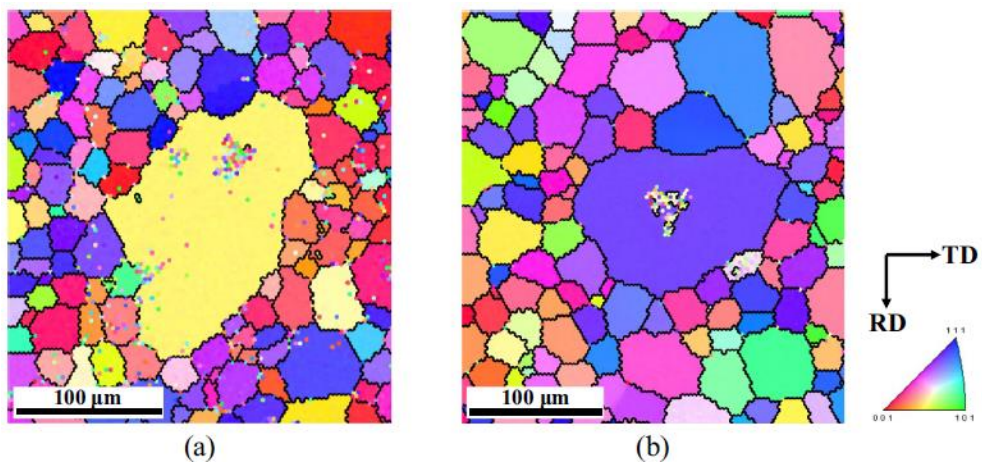
Fig. 2.3. EBSD IPF maps of the polished surface of the specimens after indentation and heat treatment. The indentation loads were (a) 0.2 kgf and (b) 0.5 kgf.
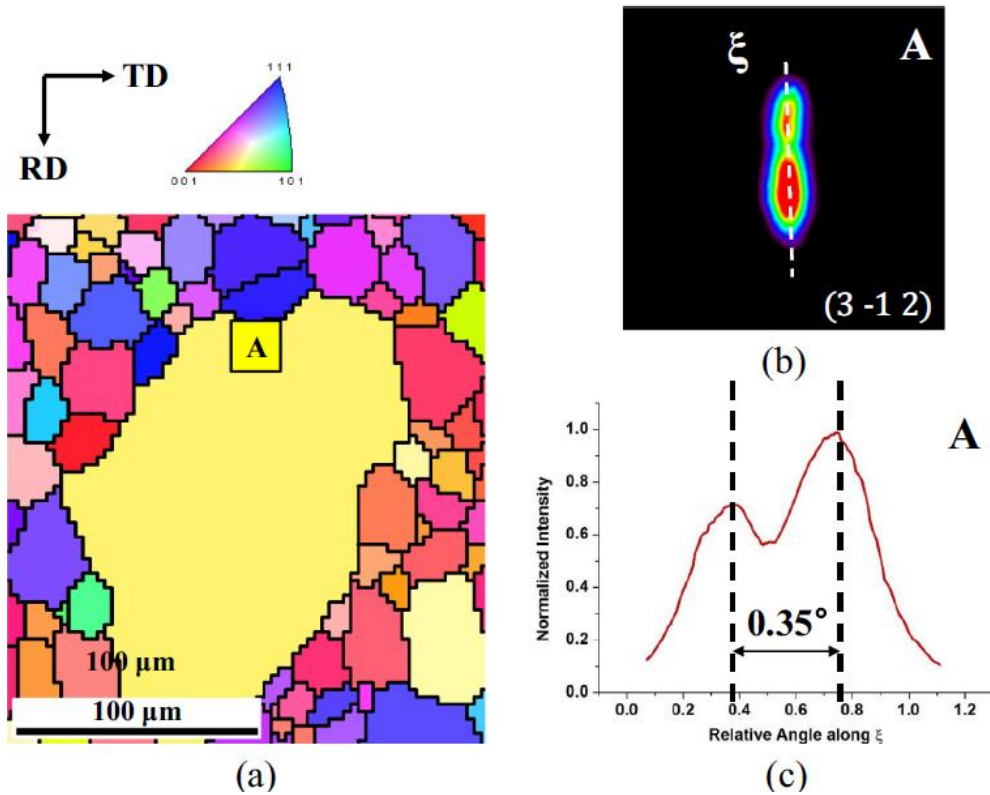
Fig. 2.4. (a) Synchrotron XMD IPF map of the polished surface after the specimen was indented under 0.2 kgf and heat treated, (b) splitting of Laue diffraction beam in $\theta - \chi$ space at the area of 'A' of the abnormally-growing yellow grain in Fig. 2.4(a), and (c) its intensity profile along the ξ direction.
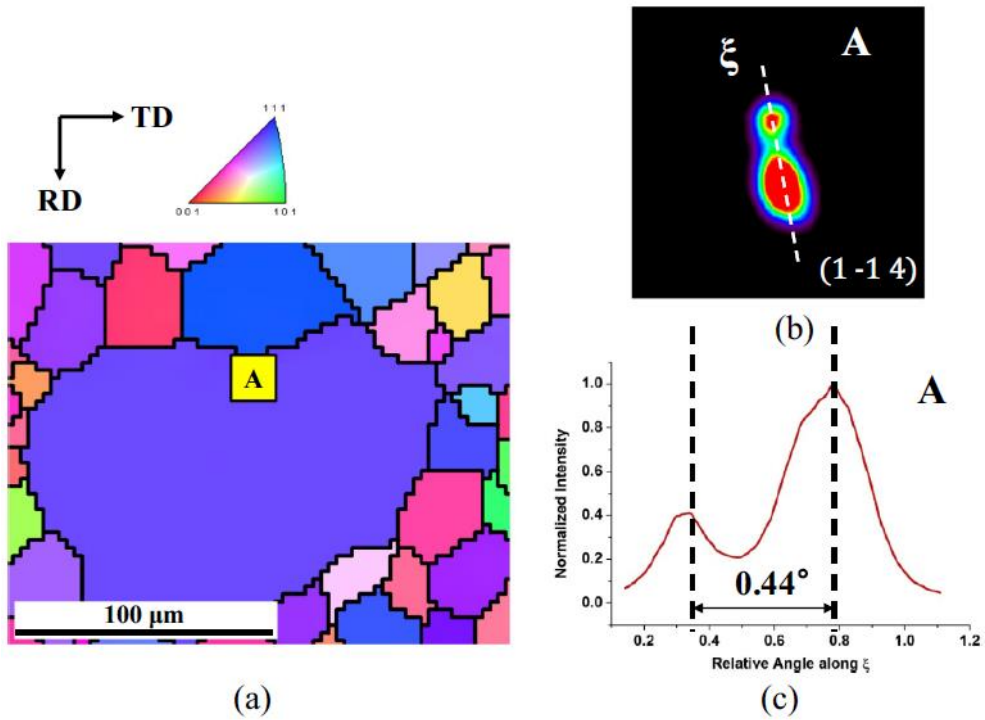
Fig. 2.5. (a) Synchrotron XMD IPF map of the polished surface after the specimen was indented under 0.5 kgf and heat treated, (b) splitting of Laue diffraction beam in $\theta - \chi$ space at the area of 'A' of the abnormally−growing indigo−blue grain in Fig. 2.5 (a), and (c) its intensity profile along the ξ direction.
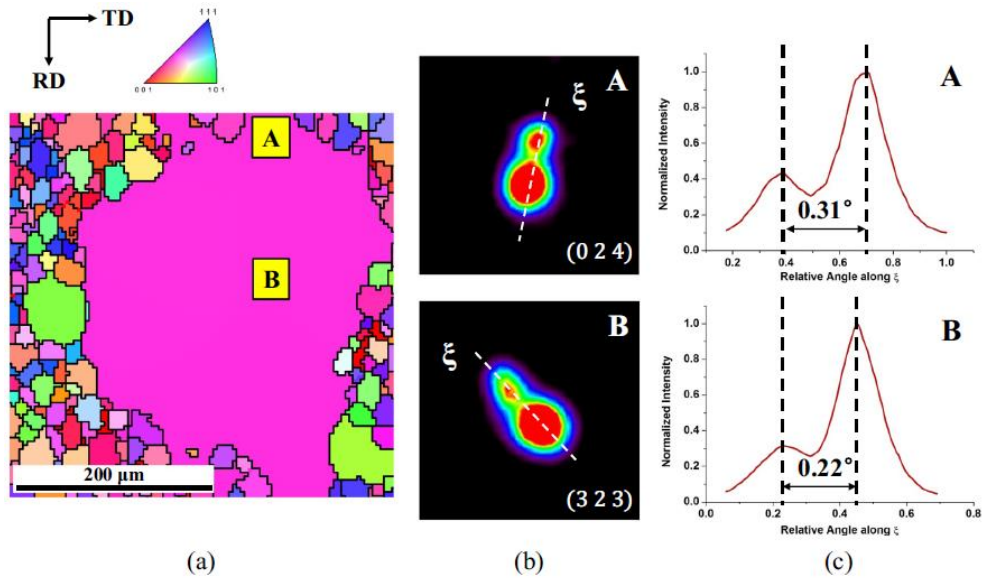
Fig. 2.6. (a) Synchrotron XMD IPF map of the polished surface after the specimen was indented under 2 kgf and heat treated, (b) splitting of Laue diffraction beams in $\theta - \chi$ space at the areas of 'A' and 'B' in the abnormally−growing magenta−purple grain in Fig. 2.6(a), and (c) their intensity profiles along the ξ direction.
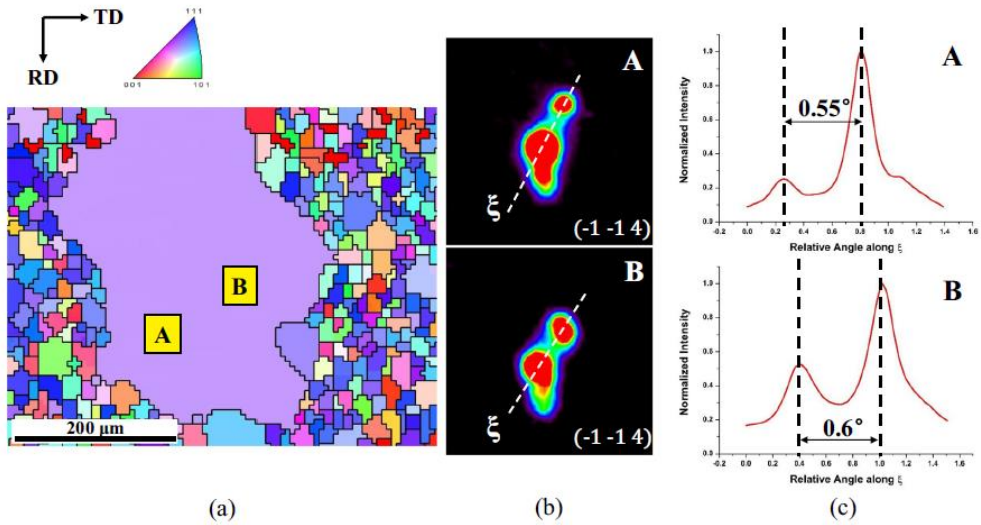
Fig. 2.7. (a) Synchrotron XMD IPF map of the polished surface after the specimen was indented under 3 kgf and heat treated, (b) splitting of Laue diffraction beams in $\theta - \chi$ space at the areas of 'A' and 'B' in the abnormally-growing violet-purple grain in Fig. 2.7(a), and (c) their intensity profiles along the ξ direction.
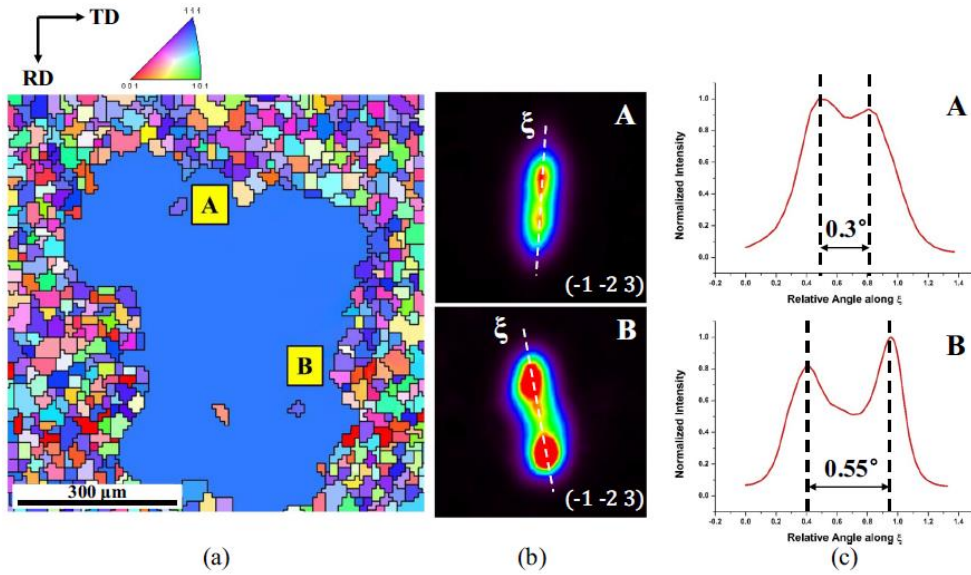
Fig. 2.8. (a) Synchrotron XMD IPF map of the polished surface after the specimen was indented under 6 kgf and heat treated, (b) splitting of Laue diffraction beams in $\theta - \chi$ space at the areas of 'A' and 'B' in the abnormally-growing blue grain in Fig. 2.8(a), and (c) their intensity profiles along the ξ direction.
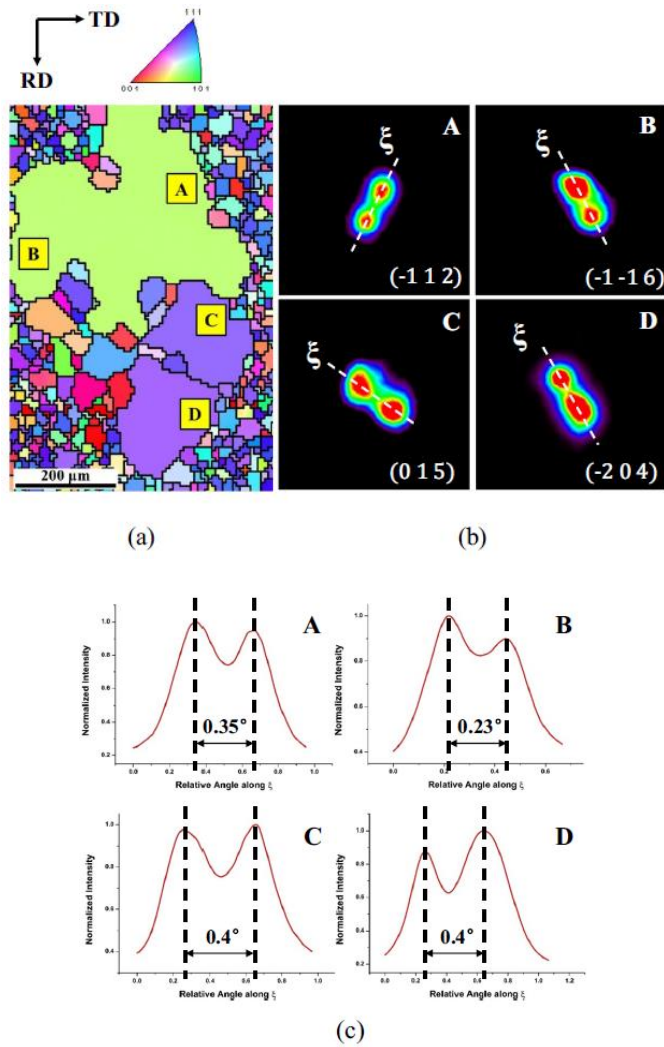
Fig. 2.9. (a) Synchrotron XMD IPF map of the polished surface after the specimen was indented under 12 kgf and heat treated, (b) splitting of Laue diffraction beams in $\theta - \chi$ space at the areas of 'A' and 'B' in the abnormally−growing leaf−green grain, 'C' in the amethyst−purple grain and 'D' the in pansy−purple grain in Fig. 2.9(a), and (c) their intensity profiles along the ξ direction.
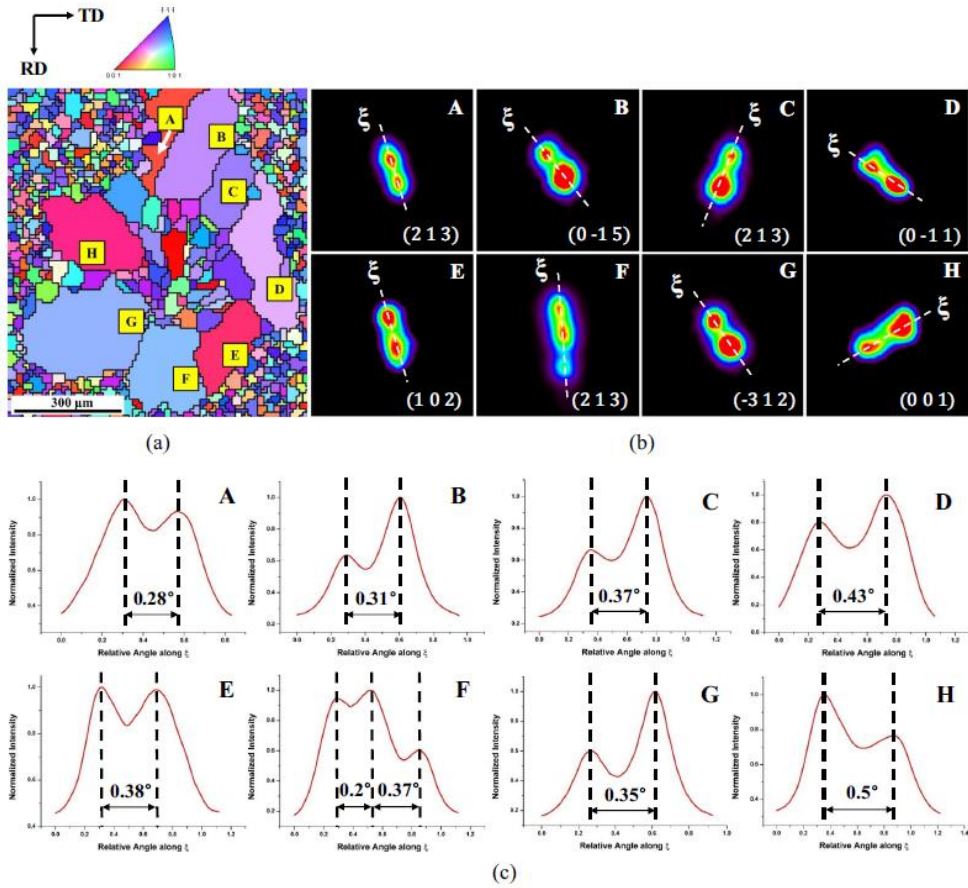
Fig. 2.10. (a) Synchrotron XMD IPF map of the polished surface after the specimen was indented under 18 kgf and heat treated, (b) splitting of Laue diffraction beams in $\theta - \chi$ space at the areas of A ~ H in the abnormally−growing grains in Fig. 2,10(a), and (c) their intensity profiles along the ξ direction.

2.4 Discussion

For all indentation loads chosen in this study, AGG occurred during heat treatment. For indentation loads less than 0.2 kgf, however, AGG did not occur. This result indicates that AGG can be induced by indentation if the loads are high enough. This means that we can generate AGG by indentation in the local area where we want.

However, the AGG induced by indentation can be regarded as the dominant growth by strain-induced boundary migration (SIBM). In relation to this possibility, Citrawati et al. [48] studied the effect of rolling on AGG of Goss grains in a Fe-3.5%Si steel and showed that rolling induced the appreciable growth of non-Goss oriented grains, which replaced the small matrix grains completely. As a result, some non-Goss oriented grains grew as large as Goss oriented grains. Due to the dominant growth of non-Goss oriented grains, after annealing for 60 min at 900°C a strong Goss texture was not evolved in cold-rolled samples whereas a strong Goss texture was evolved in the as-received sample without rolling. The role of small deformation in inducing AGG was also reported by Koo et al. [49] and Cho et al. [50]. These results are similar to ours in that small deformation induces AGG or dominant growth of non-Goss oriented grains.

Therefore, there are two possibilities for the cause of AGG induced by small deformation such as indentation and cold rolling. One possibility would be the SIBM as suggested by Citrawati et al.

[48], Koo et al. [49] and Cho et al. [50]. The other possibility would be that sub-boundaries are formed during annealing after indentation or cold rolling and AGG occurs by sub-boundary enhanced SSW. In identifying the AGG mechanism, it is important to clarify which of these two possibilities is correct.

 In clarifying these two possibilities, it should be noted that AGG was not induced when the indention load was less than 0.2 kgf as mentioned earlier. More specifically, the indentation loads of 0.01 kgf, 0.05 kgf and 0.1 kgf did not induce the dominant growth although the deformation by indentation was clearly revealed by SEM. Fig. 2.11 shows the result of the indentation load of 0.1 kgf. Fig. 2.11a, 2.11b and 2.11c shows the EBSD IPF maps of the polished surface of the specimens respectively after indentation, after heat treatment of the indented specimen for 10 min at 860°C and after heating of the same specimen to 1080°C at 5°C/min and being held for 0 s. Fig. 2.11d shows the SEM image of Fig. 2.11c, which reveals the spherical indented area. Considering the grain size, the step size of the EBSD was 4 μm. Although the plastic deformation is evident in Fig. 2.11d, such deformation or strain did not induce the dominant growth not only after heat treatment for 10 min at 860°C but also after heating to 1080°C at 5°C/min, in which condition the dominant growth occurred at the indentation load above 0.2 kgf as shown in Figs. 2.3-2.10.

 Considering that AGG occurs or does not occur, depending on the indentation load, it would be difficult to explain the effect of the

31

small deformation on AGG by SIBM. According to the mechanism of sub-boundary induced SSW, however, AGG depend on whether sub-boundaries are formed or not, not depending on whether deformation (or strain) is made or not. If the indentation load less than 0.2 kgf is not enough to form sub-boundaries, the mechanism of sub-boundary induced SSW would not work and AGG would not occur. Therefore, Fig. 2.11 seems to support the mechanism of sub-boundary enhanced SSW.

In order to examine the possible cause of the deformation-induced AGG further, the sample was observed after indentation with a load of 2 kgf and after annealing the indented specimen for 10 min at 860°C. It should be noted that the indentation load of 2 kgf induced AGG as shown in Fig. 2.6. The EBSD IPF maps are shown in Fig. 2.12a and 2.12b respectively after indentation and annealing. The step size of the EBSD was 3.5 μm. In Fig. 2.12a, the indented area is shown by tiny dots, which are the error points of the EBSD. In Fig. 2.12b, there is still an area of tiny dots, which are attributed to the non-flat surface due to indentation, failing to match the related Kikuchi patterns as mentioned earlier. If deformation-induced AGG occurs by SIBM, the non-deformed strain free grains surrounding the indented area are expected to grow into the center of the deformed area, resulting in an elongated shape. However, Fig. 2.12b shows that a little bit larger grains are formed inside the indented area instead of coming from the outside. Besides, the number of strain-free grains is expected to be large because numerous matrix

grains surround the indented area. But the number of abnormally-growing grains in Figs. 2.3-2.10 is only a few. Further, abnormally-growing grains have sub-boundaries without exception. Therefore, these results support the possibility that deformation-induced AGG is caused by sub-boundary enhanced SSW.

If this possibility is correct, sub-boundaries could be made by other means such as laser annealing of the local area, AGG can be induced also. There are some preliminary experimental results on this [51].

It is noticeable that abnormally-growing grains induced by indentation have non-Goss orientations. Conventional mechanisms for Goss AGG suggest that Goss grains have a growth advantage because they have the high percentage of high mobility [21-23] or low energy boundaries [24-28] with matrix grains. This means that the growth advantage of Goss grains comes from the matrix grains, which are in favorable misorientations to make high mobility or low energy boundaries with Goss grains. However, abnormally-growing grains induced by indentation shown in Figs. 2.4-2.10 have random orientations rather than any specific orientation. This result implies that the growth advantage of abnormally-growing grains induced by indentation does not come from the matrix grains but from the indented grain itself. Then, where does the growth advantage of the indented grain come?

In relation to this question, synchrotron XMD analyses show that all abnormally-growing grains induced by indentation have sub-

boundaries whereas all matrix grains did not without exception. This implies that sub−boundaries should provide the growth advantage for the indented grain. Then, a question arises as to how the sub−boundaries formed by indentation provide the growth advantage. The answer can be given by the mechanism of sub−boundary enhanced SSW [29−32, 37, 52−55], where grains with sub−boundaries have a much higher probability to grow by wetting along the triple junction line than those without sub−boundaries. This growth advantage by sub−boundaries was confirmed by computer simulations [36−39] and the existence of sub−boundaries in abnormally−growing grains was confirmed by experiments [33−35, 42].

  Then, how are the sub−boundaries formed by indentation and heat treatment? In the region of the plastic deformation made by indentation, recrystallization or recovery can occur during heating. When the amount of stored energy is high enough, recrystallization would occur during heat treatment. In this case, sub−boundaries would not be formed. When the amount of stored energy is not high enough, however, recovery can occur. In the recovery process, dislocations can be arranged to make sub−boundaries. One or more sub−boundaries seem to be formed in one grain, which is confirmed by the experiment results of Figs. 2.4−2.10, where one or two regions of sub−boundaries were observed in one abnormally−growing grain.

  When the indentation load was increased to 12 and 18 kgf, the

deformed area becomes larger and recovery would occur in a larger area. Then, sub-boundaries would be formed in more than one grain. As a result, more than one grains grow abnormally as shown in Figs. 2.9 and 2.10.
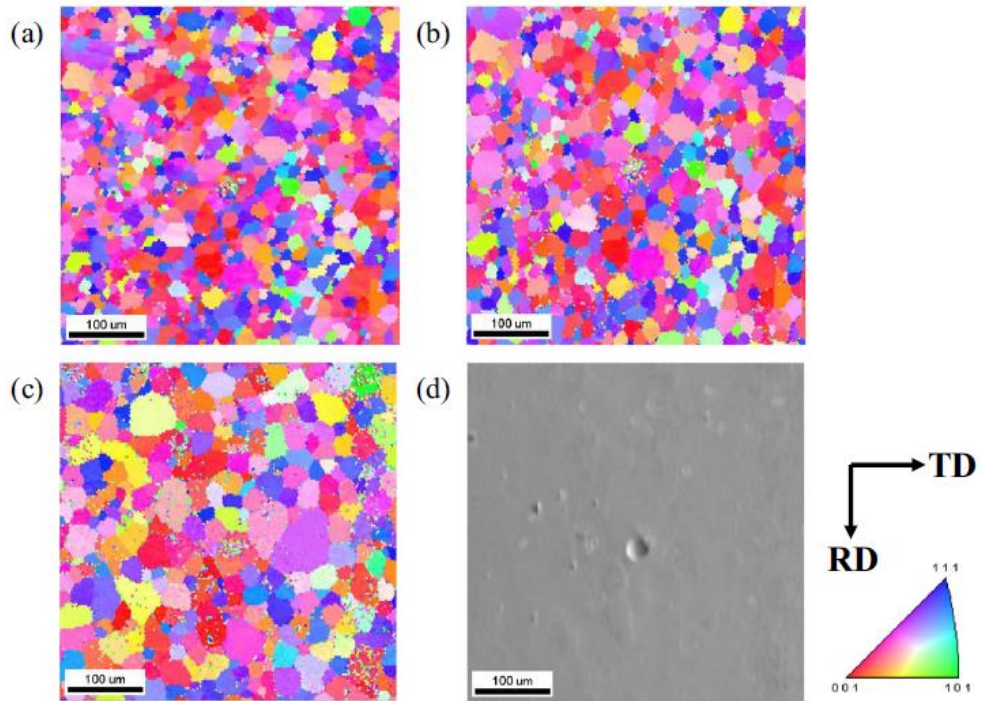
Fig. 2.11. EBSD IPF maps and SEM image of the polished surface of the specimens (a) after indentation with a load of 0.1 kgf, (b) after heat treatment of the indented specimen for 10 min at 860℃, (c) after heating of the same specimen to 1080℃ at 5℃/min and being held for 0 s, and (d) the SEM image of (c).
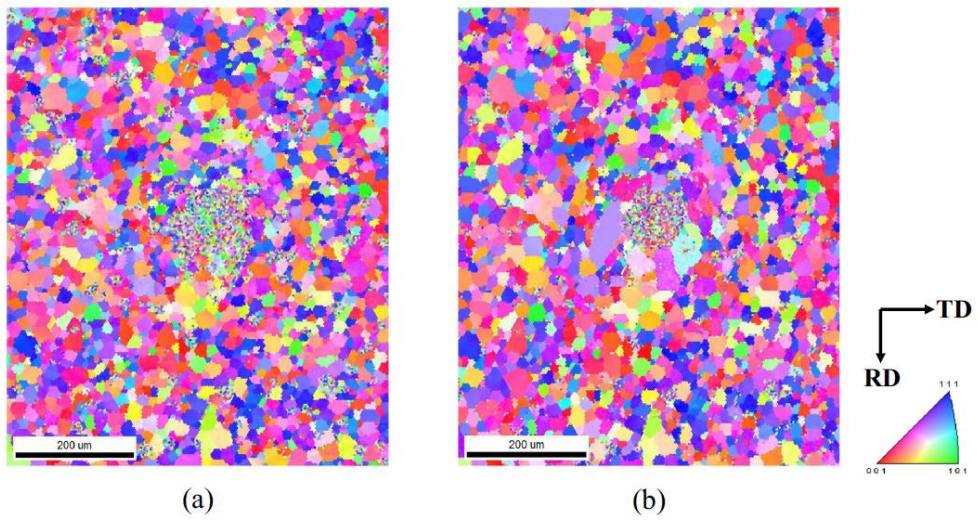
Fig. 2.12. EBSD IPF maps of the polished surface of the specimens (a) after indentation with a load of 2 kgf and (b) after heat treatment of the indented specimen for 10 min at 860ºC.

2.5 Conclusion

 AGG of non-Goss grains was induced by applying local deformation using indentation in Fe-3%Si steel. It is observed that AGG occurred around the indentation area during heat treatment. It is revealed by synchrotron XMD that all of these abnormally grown grains have orientations different from Goss grains. Also, these abnormally-growing grains had sub-boundaries inside them with very low misorientation angle below 0.6°, whereas other matrix grains did not have sub-boundaries without exception. It is suggested that sub-boundaries could be formed around the indented area by the recovery process during heating and played a decisive role in inducing AGG of non-Goss grains.

Chapter. 3 Effect of sub-boundary angle magnitude on abnormal grain growth behavior

3.1 Introduction

According to SSW mechanism, AGG can easily occur when a sub-boundary with low energy is in a wetting condition (Fig. 1.2). Even among the sub-boundaries, the grain which has a low energy sub-boundary, will grow faster than the grain which has a high energy sub-boundary (Fig 3.1). In chapter 2, the sub-boundaries had different angles. In general, low misorientation angles, such as sub-boundaries, have less grain boundary energy as the smaller the angle. That is, grain with a small sub-boundaries angle will be more easily satisfied with the wetting condition than grain with a larger sub-boundary angle. If this hypothesis is correct, the larger the grains should have the smaller the sub-boundary angle when the sub-boundary angle is identified between the grains that have grown to different sizes. Therefore, the purpose of this study is to check the growth rate of AGG by the difference of grain boundary energy by 3-dimensional MC simulation and to check the sub-boundary angle of the abnormally-growing grains where AGG occurred in different sizes within the same specimen.
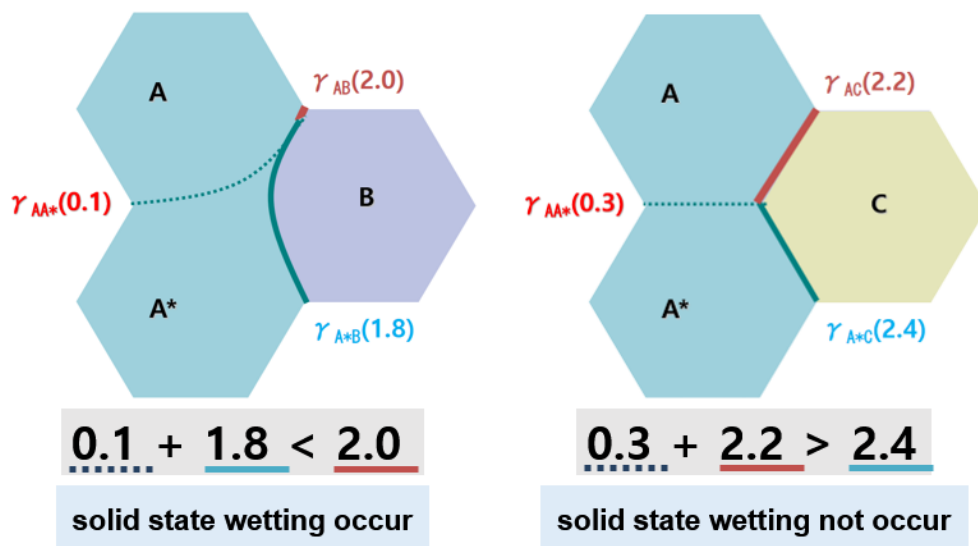
Fig. 3.1. Schematic diagram of SSW with grain boundary energy.

3.2 Experiment procedure

 To how the sub−boundary angle affects AGG, parallel 3−dimensional MC simulations were performed on a simple cubic lattice using a method similar to that reported by Park et al. In the simulations, 160 × 160 × 160 cubic lattice sites were used with periodic boundary conditions in the x, y and z directions. Each site has a grain number, and a grain consists of sites with the same grain number. Each grain number has a crystallographic orientation with Bunge Euler angles ($\varphi 1$, Φ, $\varphi 2$). To make the 3−dimensional MC simulation as realistic as possible, 8000 initial grain orientations determined by EBSD measurements of Fe−3%Si steel after primary recrystallization were used.

 The misorientation angle between two adjacent grains can be calculated from Euler angles. Since a cubic lattice has 24 symmetries, one set of Euler angles has 24 matrix elements of directional cosines. The matrix multiplication of two Euler angles of adjacent grains produces 24 × 24 matrix elements among which the matrix element with the minimum angle corresponds to the misorientation angle of adjacent grains. The grain boundary energy is determined from the misorientation angle by the following equations derived by Read−Shockley equation [56].

$$E(S_i, S_j) = \begin{cases} E_0 \frac{\theta}{\theta_{RS}}\left[1 - \ln\left(\frac{\theta}{\theta_{RS}}\right)\right], & \theta < \theta_{RS} \quad \text{(low angle boundary)} \\ r', & \theta \geq \theta_{RS} \quad \text{(high angle boundary)} \\ E_{CSL} \frac{w}{v_m}\left[1 - \ln\left(\frac{w}{v_m}\right)\right], & \frac{w}{v_m} < 1 \quad \text{(CSL boundary)} \end{cases}$$

(3.1)

where S_i and S_j are the orientations of adjacent grains and $E(S_i, S_j)$ is the grain boundary energy. θ is the misorientation angle, and θ_{RS} is the maximum misorientation angle of the low angle boundary, 15o. r' is the energy of the high angle boundary. w is the deviation angle between the real misorientation and the misorientation of the exact CSL boundary, and w_m is the maximum deviation angle, $\theta_{RS}/\Sigma^{\frac{1}{2}}$ [57, 58]. E_{CSL} is the grain boundary energy of the exact CSL boundary. E_0, E_{CSL} and r' are set by the result of the mesoscale simulation performed by Kim et al. [57, 59]. In evaluating the grain boundary energy, the effect of the inclination angle was not considered.

The grain boundary energy of a lattice site was obtained by the following equation:

$$E = \sum_n J(S_i, S_j)[1 - \delta_{ij}]$$

(3.2)

where n is the number of nearest neighbors having a different orientation and δ_{ij} is the Kronecker delta function. The first, second and third 26 nearest neighbors are considered to determine the grain boundary energies. One of the 26 neighbor orientations was randomly selected, and the energy of the states before and after the orientation change was compared. When the energy change is zero or negative, the orientation change is accepted. When the energy change is positive, the orientation change is determined by the Boltzmann probability, P, as follows:

$$P = \exp\left(-\frac{\Delta E}{k_B T}\right),$$

(3.3)

where ΔE is the energy change, kB is the Boltzmann constant and T is the lattice temperature. As mobility data were not available, the grain boundary mobility was assumed to be the same.

To incorporate precipitates into the simulation, 10% of all lattice sites are assigned for precipitates which have an orientation different from those of all the grains. Each precipitate has only one site. The locations of the particles are randomly chosen and they are not allowed to reorient or move. Therefore, the size of the precipitates is fixed, as described in detail elsewhere [60, 61]. During the simulation, the precipitates, which are located at triple junctions or quadruple points, are gradually removed with varying probability of between 1 and 2% at every 50th MCS. This gradual removal of precipitates from triple junctions or quadruple points is to consider the real situation for the dissolution of precipitates during heating for secondary recrystallization because the dissolution kinetics is much faster in triple junctions or quadruple points, which have high diffusion paths.

At the small misorientation angles, such as sub−boundary, the size of the grain boundary angle and the grain boundary energy are proportional, so the MC simulation was performed by changing the grain boundary energy. A total of 10,000 Monte Carlo steps (MCS) were carried out, and the initial structure consisted of 8,000 grains of the same size and the orientation of the Grains was chosen

randomly each. The matrix grain boundary energy was distributed from 1 to 1.4 according to their misorientation. The eight central grains consist of sub-boundary with energies of 0.001, 0.0015 and 0.005, with a 10% chance of that matrix grains will have low energy boundary. These energies were determined based on experimental results. The energy range of matrix grains was calculated by mesoscale grain growth simulations considering the grain boundary misorientation and inclination in iron [57]. Also, the sub-boundary energy was calculated by the Read-Schockley model [56] from the dislocation spacing of the sub-boundaries observed in Park et al. work [36, 37].

 The experiment was performed with Fe-3%Si steel with aluminum nitride added as a grain growth inhibitor was used to examine the AGG changes with the effect of the sub-boundary angle. The Fe-3%Si steel ingot was hot-rolled to 2.3 mm and cold-rolled to 0.3 mm. Then, it was recrystallized at 850°C for 150 s for primary recrystallization. Then, it was recrystallized at 850°C for 150 s for primary recrystallization. The surface of some specimens was indented by a Brinell indenter with a load of 2 kgf to check AGG generated with various method. The secondary recrystallization was carried out in the tube furnace under flowing hydrogen (99.9999%) to prevent the specimens from oxidizing. To observe the initial microstructure of secondary recrystallization, the specimens were heated to 1080° at 5°C/min, held for 0 min and transferred from the hot zone to the cold zone in the tube furnace.

Besides, in order to check the sub-boundary angle of Goss grains after secondary recrystallization, the other specimen was heated to 1080° at 5°C/min, held for 24 hr. These specimens were polished to observe their microstructure and analyzed by EBSD (EDAX, Hikari). Considering the grain size, the step size of the EBSD was 3.5 μm.

To check the possibility that abnormally-growing grains might have sub-boundaries, synchrotron white beam (XMD) experiments were conducted on 4B beamline at the Pohang Accelerator Laboratory (PAL) to determine the crystallographic orientations of grains in the microstructure. The abnormally-growing Goss grain was scanned two dimensionally with a step size of 3-4 μm. Laue diffraction images were collected at each step so that approximately maximum 10,000 images per one specimen were used for analysis. The other settings were set up in the same analysis method as synchrotron XMD in Chapter 2.

3.3 Results and discussion

Fig. 3.2 shows the cross−sections of a 3−dimensional MC simulation microstructure by variation of sub−boundary energy at z = 80 after 1000, 5000 and 10000 MCS. The sub−boundary energy inside green grain is 0.001, 0.0015, and 0.005 as shown Fig. 3.2a, 3.2b and 3.2c, respectively. In Fig. 3.2a, the central green grain shows that AGG has already occurred at 1,000 MCS, and that it has continued to grow and consumed almost all grains at 10,000 MCS. In Fig. 3.2b, AGG occurred in all MCS like Fig. 3.2a. However, although the AGG phenomenon is similar to that of Fig. 3.2a, the size of the AGG is smaller by looking at the all MCS. Finally, the green grain in Fig. 3.2c is difficult to determine if AGG has occurred in 1,000MCS, but in 5,000MCS, AGG be confirmed to occur and it can be seen that AGG has occurred even more in 10,000MCS. These MC simulation results in Fig. 3.2 indicate that the larger size abnormally−growing grains have smaller the grain boundary energy.

Figs. 3.3, 3.4 and 3.5 show the results obtained by synchrotron XMD for AGG generated by indentation (Fig. 3.3) and abnormally− growing Goss grains (Figs. 3.4 and 3.5) respectively. Figs. 3.3a, 3.4a and 3.5a show the synchrotron XMD IPF map. The splitting in the region 'A' (Figs. 3.3a, 3.4a and 3.5a) and 'B' (Figs. 3.3a, 3.4a and 3.5a) occurs Laue diffraction beams respectively as shown in Figs. 3.3b, 3.4b and 3.5b. Corresponding intensity profiles of the splitting beam in the region of 'A' (Figs. 3.3a, 3.4a and 3.5a) and

'B' (Figs. 3.3a and 3.4a) are shown along the splitting direction ξ respectively in Figs. 3.3c, 3.4c and 3.5c. In other words, the beam splitting in Figs. 3.3b, 3.4b and 3.5b corresponds to the peak splitting in Figs. 3.3c, 3.4c and 3.5c. The misorientation angle of the sub-boundary can be calculated from the distance between two intensity maxima along the splitting direction ξ [46]. From the intensity profiles in Figs. 3.3c, 3.4c and 3.5c, the misorientation angles of sub-boundaries in regions of 'A' (Figs. 3.3a, 3.4a and 3.5a) and 'B' (Figs. 3.3a and 3.4a) were calculated to be respectively 0.35°, 0.42°, 0.19°, 0.2° and 0.2°. In other words, the sub-boundary angle of abnormally-growing Goss Grains is small and the sub-boundary angle of small sized abnormally-growing grains induced by indentation is large. These results, as with MC simulation results, indicate that the larger size abnormally-growing grains have smaller the grain boundary energy. However, the experimental results are statistically deficient. So the sub-boundary angle of abnormally-growing Goss grains of different sizes was also analyzed.

Fig. 3.6 show that EBSD IPF maps of the polished surface of the specimens after heat treatment. The point No. 1 is located on a small size abnormally-growing Goss grain, the point No. 2, 3 and 4 are located on a medium size abnormally-growing Goss grain and the point No. 5, 6, 7 and 8 are located on a large size abnormally-growing Goss grain. These abnormally-growing Goss grains also have splitting of Laue diffraction beams occurs exclusively,

indicating that AGG might be related with sub-boundaries. These abnormally-growing Goss grains show the beam splitting as designated as 'A', 'B', 'C' and 'D' in Figs. 3.7a, 3.8a and 3.9a respectively. The corresponding beam splittings are shown respectively in Figs. 3.7b, 3.8b and 3.9b. The corresponding intensity profiles are shown respectively in Figs. 3.7c, 3.8c and 3.9c. The misorientation angles of the sub-boundaries in regions 'A' is $0.41°$ as shown Fig. 3.7c and the misorientation angles of the sub-boundaries in regions 'A', 'B' and 'C' are $0.35°$, $0.3°$ and $0.35°$ respectively as shown Fig 3.8c. Finally the misorientation angles of the sub-boundaries in regions 'A', 'B', 'C' and 'D' are $0.26°$, $0.23°$, $0.27°$ and $0.24°$ respectively as shown Fig 3.9c.

Meanwhile, Fig. 3.10 shows that Goss grain, which has finished the second recrystallization and the point No. 1 and 2 were analyze for sub-boundaries angles by synchrotron XMD. Fig. 3.11a, and 3.12a show the synchrotron XMD IPF map. The splitting in the region 'A' and 'B' occurs Laue diffraction beams respectively as shown in Figs. 3.11b, and 3.12b. Corresponding intensity profiles of the splitting beam in the region of 'A' and 'B' are shown along the splitting direction ξ respectively in Figs. 3.11c, and 3.12c. In other words, the beam splitting in Figs. 3.11b, and 3.12b corresponds to the peak splitting in Figs. 3.11c, and 3.12c. The misorientation angle of the sub-boundary can be calculated from the distance between two intensity maxima along the splitting

direction ξ [46]. From the intensity profiles in Figs. 3.11c, and 3.12c, the misorientation angles of sub-boundaries in regions of 'A' and 'B' were calculated to be respectively 0.05°, 0.02°, 0.07° and 0.06°. These sub-boundary angles are very small compared to the previous results.

The table 3.1 show that average sub-boundary angles.

	Laue peak index	Sub-boundary angle	Average
Indentation AGG	$(0\,\bar{2}\,4)$	0.35°	0.39°
	$(2\,\bar{2}\,4)$	0.42°	
Small Goss grain AGG	$(\bar{1}\,\bar{1}\,6)$	0.41°	0.41°
Medium Goss grain AGG	$(\bar{2}\,\bar{3}\,3)$	0.35°	0.33°
	$(0\,0\,2)$	0.3°	
	$(1\,\bar{1}\,4)$	0.35°	
Large Goss grain AGG	$(\bar{3}\,0\,1)$	0.19°	0.23°
	$(\bar{2}\,2\,6)$	0.2°	
	$(5\,\bar{1}\,2)$	0.2°	
	$(\bar{5}\,\bar{1}\,4)$	0.26°	
	$(1\,\bar{5}\,4)$	0.23°	
	$(0\,1\,5)$	0.27°	
	$(2\,\bar{2}\,6)$	0.24°	
Secondary recrystallization Goss Grain	$(2\,0\,2)$	0.05°	0.05°
	$(2\,1\,3)$	0.02°	
	$(4\,0\,6)$	0.07°	
	$(3\,0\,3)$	0.06°	

Table. 3.1. Average of sub-boundary angles.

The average of sub-boundary angles of abnormally-growing grains induced by indentation and small size abnormally-growing Goss grains are 0.39° and 0.41°. Besides, the average of sub-boundary angle of medium size abnormally-growing Goss grains is

0.33°. Finally, the average of sub-boundary angle of large size abnormally-growing Goss grains is 0.23°. In addition, the average of sub-boundary angle of Goss grains which completed secondary recrystallization is 0.05°. This is the result of re-experimental confirmation that the larger size abnormally-growing grains have smaller the grain boundary energy.
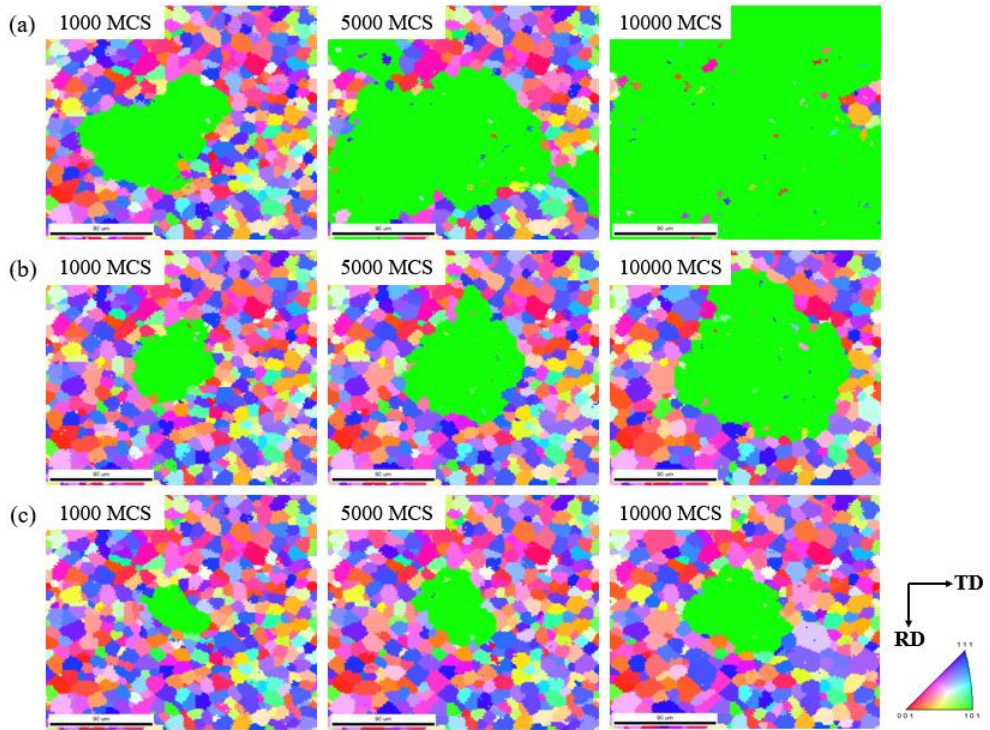
Fig. 3.2. Cross−sections of 3−dimensional MC simulation microstructure by variation of sub−boundary energy at z = 80 after 1000, 5000 and 10000 MCS. The sub−boundary energy inside green grain is (a) 0.001, (b) 0.0015 and (c) 0.005 respectively. The other grain boundaries vary from 1 to 1.4.
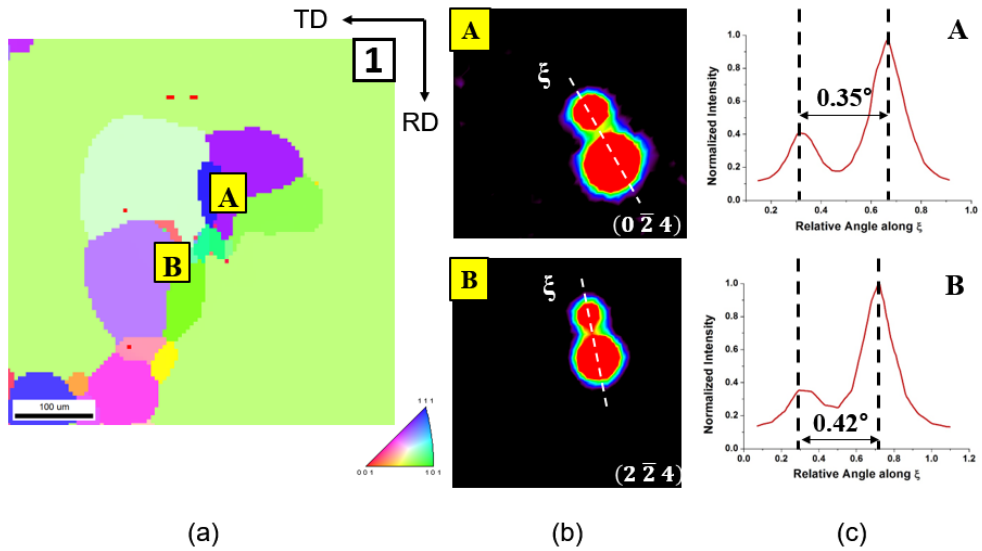
Fig. 3.3. (a) Synchrotron XMD IPF map of the polished surface after heat treated, (b) splitting of Laue diffraction beams in $\theta - \chi$ space at the area of 'A' and 'B' of the abnormally−growing grain induced by indentation in Fig. 3.3(a), and (c) its intensity profiles along the ξ direction.
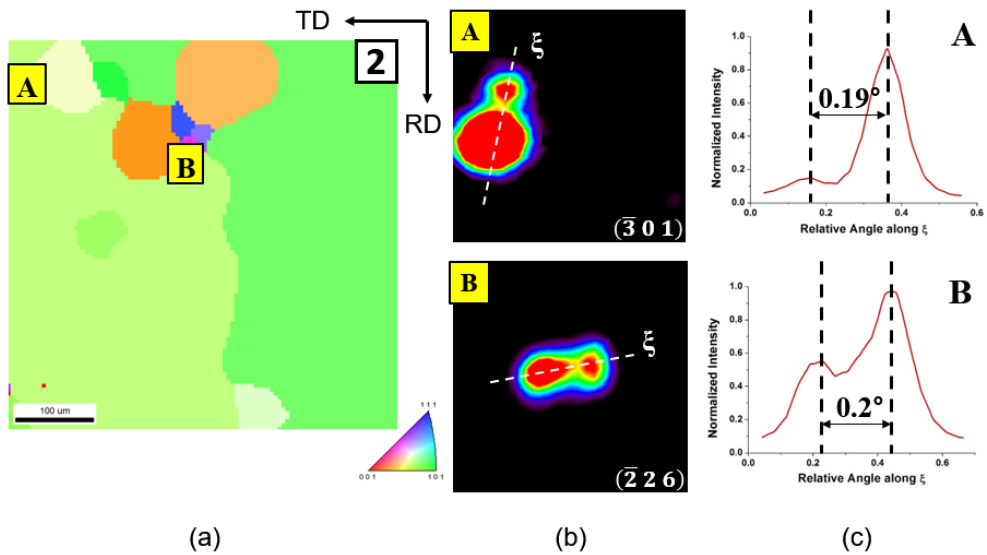
Fig. 3.4. (a) Synchrotron XMD IPF map of the polished surface after heat treated, (b) splitting of Laue diffraction beams in $\theta - \chi$ space at the area of 'A' and 'B' of the abnormally−growing Goss grain in Fig. 3.4(a), and (c) its intensity profiles along the ξ direction.
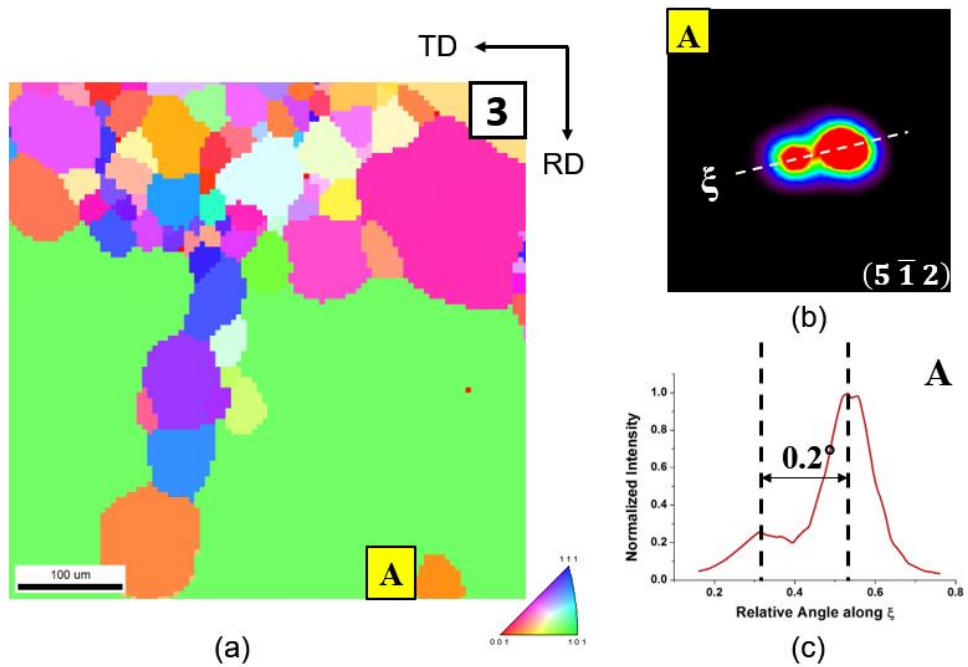
Fig. 3.5. (a) Synchrotron XMD IPF map of the polished surface after heat treated, (b) splitting of Laue diffraction beams in $\theta - \chi$ space at the area of 'A' of the abnormally−growing Goss grain in Fig. 3.5(a), and (c) its intensity profiles along the ξ direction.
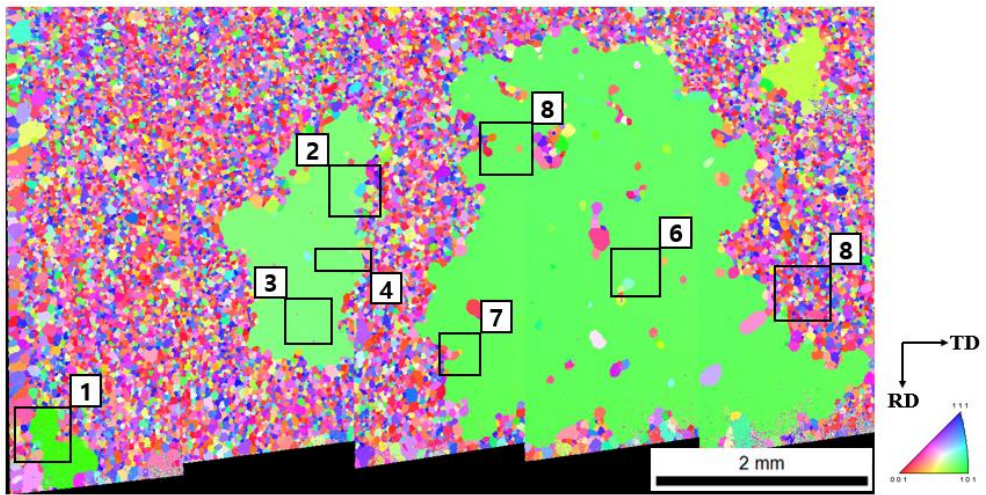
Fig. 3.6. EBSD IPF maps of the polished surface of the specimens after heat treatment. The point No. 1 is located on a small size Goss grain, the point No. 2, 3 and 4 are located on a medium size Goss grain and the point No. 5, 6, 7 and 8 are located on a large size Goss grain.
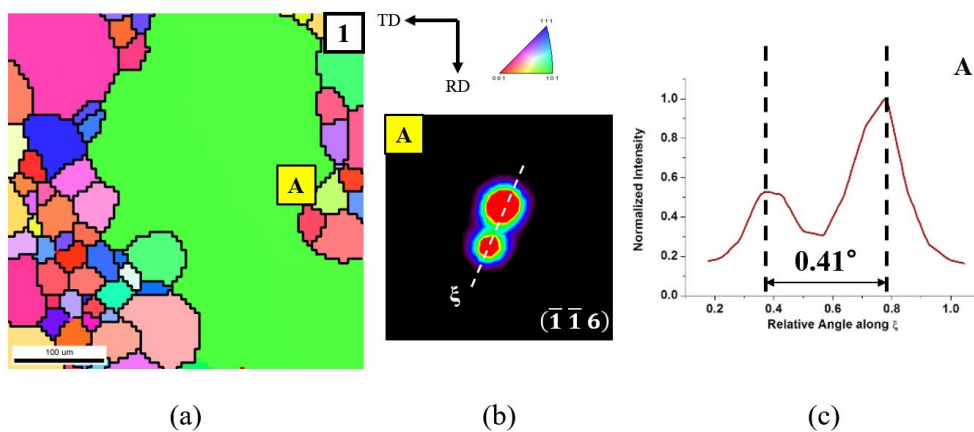
Fig. 3.7. (a) Synchrotron XMD IPF map of the polished surface after heat treated, (b) splitting of Laue diffraction beam in $\theta - \chi$ space at the area of 'A' of the small size abnormally−growing Goss grain in Fig. 3.7(a), and (c) its intensity profile along the ξ direction.
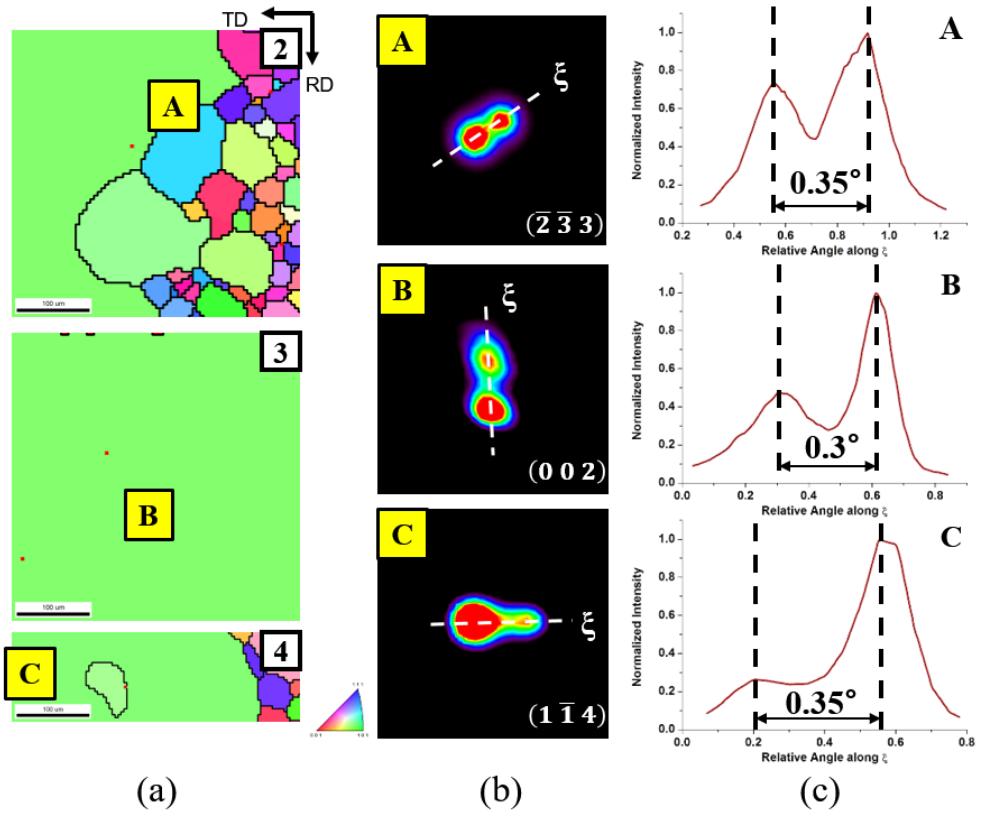
Fig. 3.8. (a) Synchrotron XMD IPF map of the polished surface after heat treated, (b) splitting of Laue diffraction beams in $\theta - \chi$ space at the areas of A ~ C in the medium size abnormally−growing Goss grain in Fig. 3.8(a), and (c) their intensity profiles along the ξ direction.
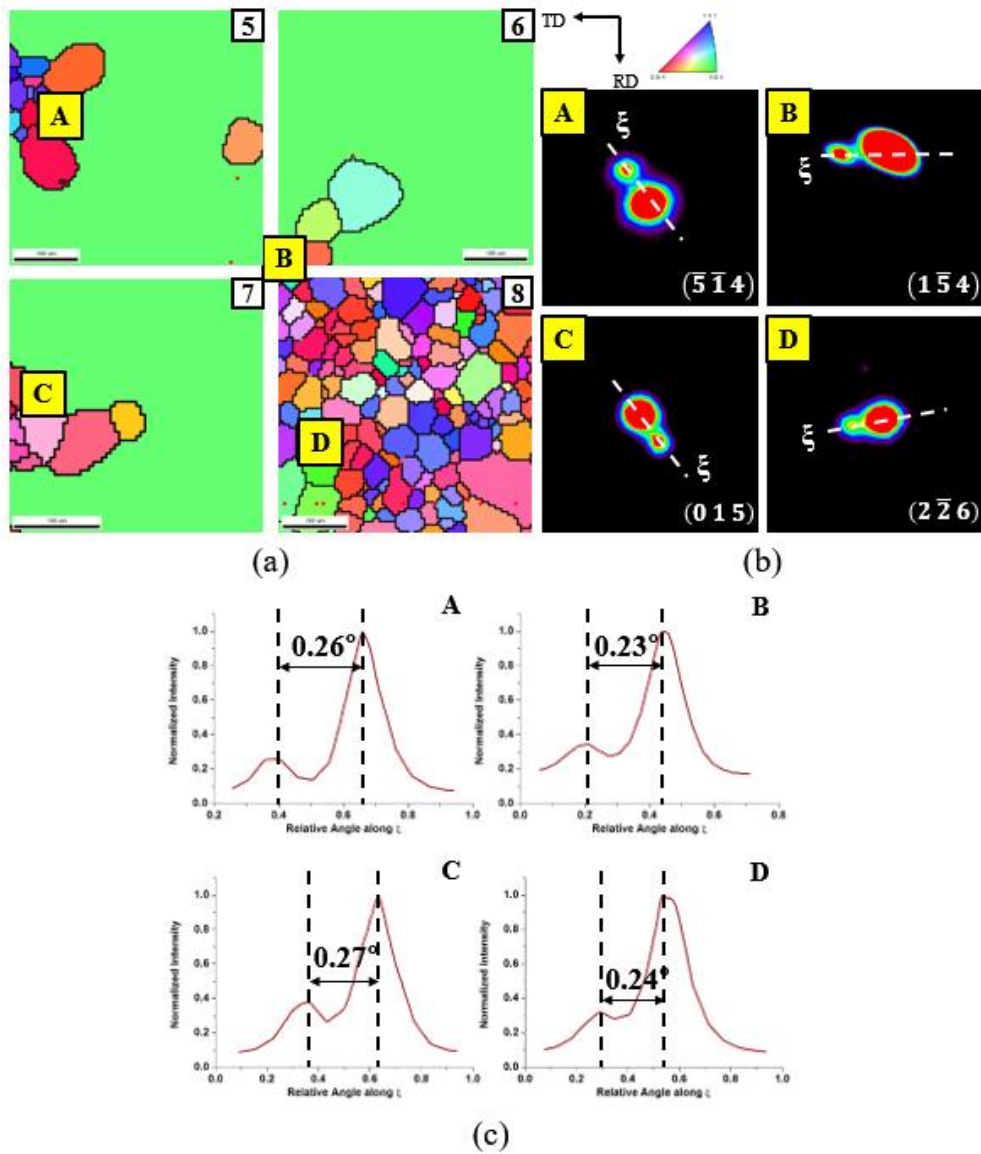
Fig. 3.9. (a) Synchrotron XMD IPF map of the polished surface after heat treated, (b) splitting of Laue diffraction beams in $\theta - \chi$ space at the areas of A ~ D in the large size abnormally-growing Goss grain in Fig. 3.9(a), and (c) their intensity profiles along the ξ direction.
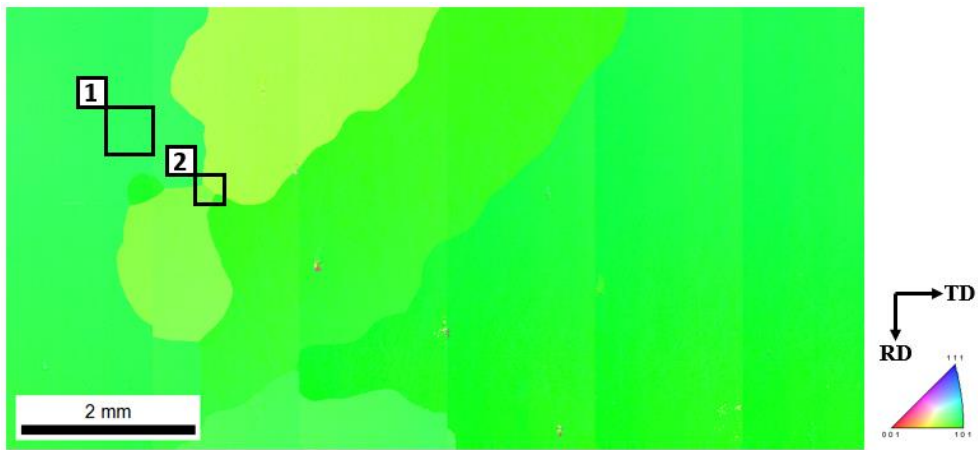
Fig. 3.10. EBSD IPF maps of the Fe-3%Si steel after secondary recrystallization.
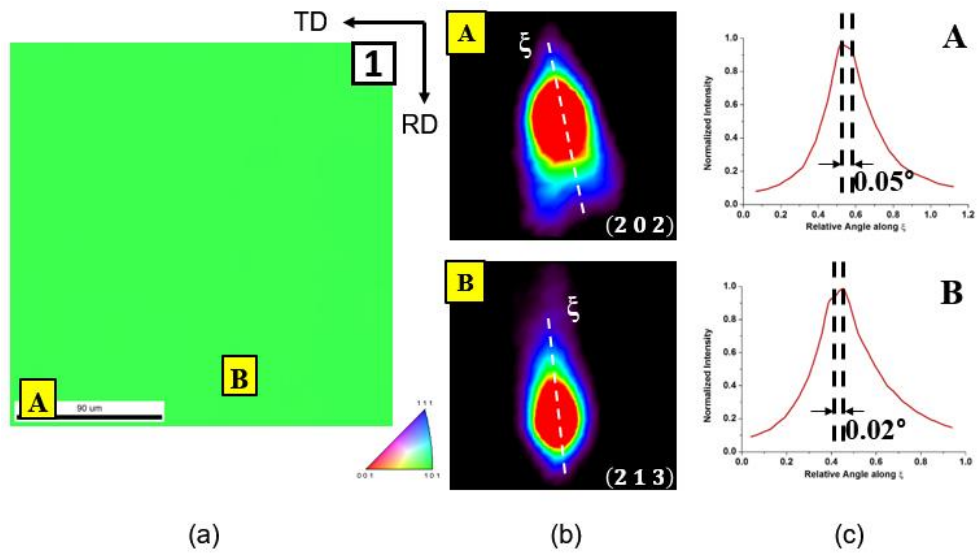
Fig. 3.11. (a) Synchrotron XMD IPF map of abnormally−growing Goss grain, (b) splitting of Laue diffraction beams in $\theta - \chi$ space at the areas of 'A' and 'B' in the abnormally−growing Goss grain in Fig. 3.11 (a), and (c) their intensity profiles along the ξ direction.
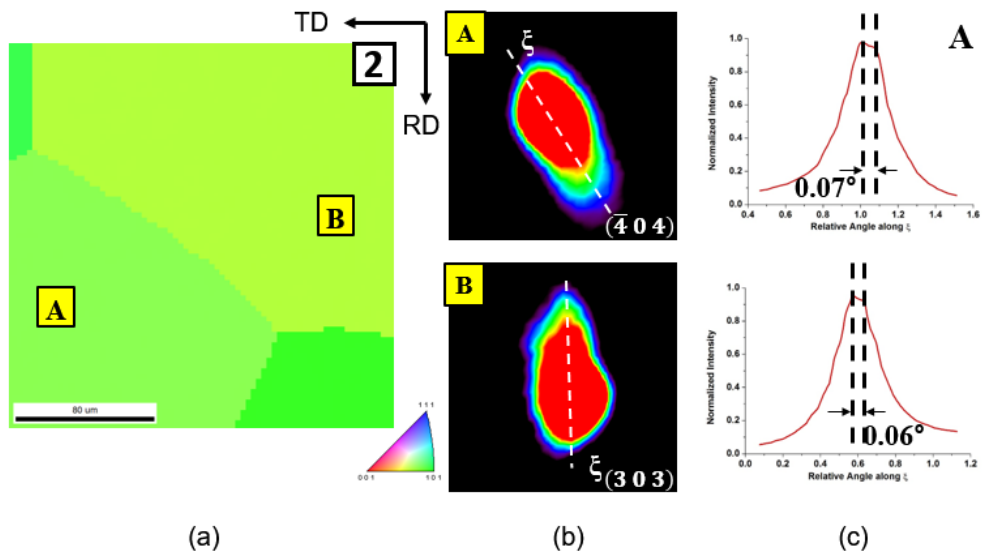
Fig. 3.12. (a) Synchrotron XMD IPF map of abnormally−growing Goss grains, (b) splitting of Laue diffraction beams in $\theta - \chi$ space at the areas of 'A' and 'B' in the abnormally−growing Goss grain in Fig. 3.12 (a), and (c) their intensity profiles along the ξ direction.

3.4 Conclusion

The one Fe−3% Si steel, after primary recrystallization, were annealed at high temperature to induce AGG. And the other Fe−3% Si steel was indented by a Brinell indenter with a load of 2 kgf to check AGG generated with various method before annealed at high temperature to induce AGG. The Goss grains undergo to AGG and these several Goss grains were analyzed using synchrotron XMD to measure sub−boundary angles. The analyses showed that all Goss grains examined had sub−boundaries with misorientations less than 1° and all matrix grains examined had no sub−boundaries. Also, small Goss grains tended to have large sub−boundary angles and vice versa. It is suggested that the sub−boundary angle should be a determining parameter of the size of abnormally−growing grains.

Chapter. 4 Ex-situ time sequential observation of Goss grains in Fe-3%Si steel

4.1 Introduction

The time sequential observation can reveal clearly that AGG occurs by SSW, and it can reveal that island and peninsular grains are formed by SSW. The reason why the ex‒situ time sequential observation was successful in aluminum alloy would be that it is resistant to oxidation. Previously, ex‒situ time sequential evolution of abnormally‒growing grains was observed in the 5052 aluminum alloy by repeating the heat treatment and observation by EBSD [35]. Such time sequential observation would be also useful in studying the formation mechanism of island and peninsular grains during AGG in Fe‒3%Si steel. However, there is a difficulty in applying the ex‒situ time sequential observation to Fe‒3%Si steel because of the surface oxidation problem. In our preliminary experiment of time sequential observation of abnormally‒growing Goss grains in Fe‒3%Si steel, however, we found out that Fe‒3%Si steel is easily oxidized when the specimen was taken out of the furnace after each heat treatment. In order to solve this problem, we removed the oxidized layer with thickness less than 1 μm by polishing. By removing the oxidized layer, abnormally‒growing Goss grains could be observed time sequentially by EBSD. The

purpose of this paper is to make the time sequential observation focusing on how island and peninsular grains are formed and shrink in abnormally−growing Goss grains in Fe−3%Si steel.

4.2 Experiment procedure

Fe-3%Si steel with aluminum nitride added as a grain growth inhibitor was used. The Fe-3%Si steel ingot was hot-rolled to 2.3 mm and cold-rolled to 0.3 mm. Then, it was recrystallized at 850°C for 150 s for primary recrystallization. To observe the ex-situ time evolution of the specimen surface during the initial stage of secondary recrystallization, the specimens after primary recrystallization were polished. The surface of some specimens was indented by a Brinell indenter with a load of 2 kgf to identify the location. The secondary recrystallization was carried out in the tube furnace under flowing hydrogen (99.9999%) to prevent the specimens from oxidizing. To observe the initial microstructure of secondary recrystallization, the specimens were heated to 1080°C at 5°C/min, held for 0 min and transferred from the hot zone to the cold zone in the tube furnace. These specimens were polished to observe their microstructure and analyzed by EBSD (EDAX, Hikari). Considering the grain size, the step size of the EBSD was 3.5 μm. After the initial microstructure of secondary recrystallization was observed and analyzed, the specimens were further heat-treated to examine the time evolution of the Goss grains, heated to 1080°C, held for 3 min or 5 min and transferred from the hot zone to the cold zone in the tube furnace.

To remove the oxide film formed on the specimen surface during the additional heat treatment, the specimens underwent the final

stage polishing for 1 min using the alumina suspension (OP−S, Struers), which would remove less than 1 μm of the surface. The alumina suspension can polish down to the depth of 0.04 μm, enabling the oxide film to be removed, which can be confirmed by the EBSD IPF map. Fig. 4.1a shows the EBSD IPF−ND map of the Fe−3%Si specimen after primary recrystallization and indentation. Fig. 4.1b shows the EBSD IPF−ND map of the specimen surface after the heat treatment at 1080°C for 0 min. Because of the surface oxidation, there are many error points in the EBSD analysis. After the final stage polishing for 1 min of the specimen for Fig. 4.1b, a clear EBSD IPF−ND map could be obtained as shown in Fig. 4.1c. Therefore, if the above procedure of heat treatment at 1080°C and final stage polishing is repeated, the ex−situ time evolution of the abnormally−growing Goss grains can be observed and analyzed by EBSD.

The sequential heat treatment for 5 min at 1080°C was repeated 6 times to examine the time evolution of Goss grains. For another set of the experiment, the sequential heat treatment for 3 min at 1080°C was repeated 3 times. To examine the time evolution of Goss grains in a shorter time interval, the third set of the experiment was done where the specimen was heat treated sequentially for 6 min, 5 min, 2.5 min, 2.5 min and 2 min, which corresponded to a total of 18 min heat treatment.
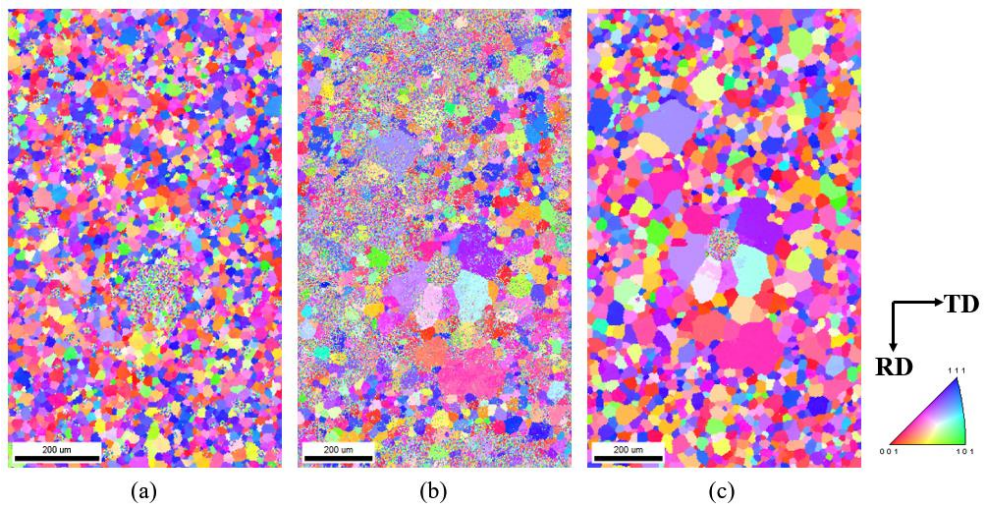
Fig. 4.1. EBSD IPF maps (a) after primary recrystallization and indentation, (b) before and (c) after polishing of Fe−3%Si steel heated to 1080℃ at 5℃/min, held for 0 min and cooled.

4.3 Results and discussion

Fig. 4.2 is EBSD IPF−ND maps showing the time evolution as to how Goss grains grew with heat treatment time. Fig. 4.2a shows three abnormally−growing Goss grains: one on the bottom left (grain A), another at the center (grain B) and the third on the bottom right (grain C). Because their color code is green or yellow green, it appears that they are near−Goss grains, even if they are not exactly Goss grain. Considering that they grew from the initial matrix grain size of 30−40 μm to ~ 500 μm or larger, they must have undergone AGG.

In Fig. 4.2b, which was evolved after 5 min heat treatment, the grain B at the center impinged with the grain A at the bottom left. As a result, many matrix grains were trapped at the bottom center of Fig. 4.2b indicated by the large black circle. Once trapped, these matrix grains shrank away relatively fast and most of them disappeared in Fig. 4.2d.

As grains B and C grew toward each other, peninsular grains indicated by the small black circle is formed as shown in Fig. 4.2b. These peninsular grains in Fig. 4.2b became island grains after another 5 min heat treatment in Fig. 4.2c as a result of the impingement between grains B and C. Another peninsular grains indicated by the black circle were formed as the grain C grew in the upper direction. Grains A and D have a similar green color in Fig. 4.2c−4.2f. However, their misorientation angle is about 7° which is a low misorientation angle. This means that grains A and D have a

similar IPF color code but are different grains.

After another 5 min in Fig. 4.2d, grains B and D almost impinged, trapping a huge amount of matrix grains indicated by the black circle. Once trapped, these matrix grains shrank fast and most of them disappeared in Fig. 4.2f. After another 5 min in Fig. 4.2e, a large grain appeared in the center of the isolated matrix grains indicated by the large black circle. This grain is identical to the A grain, which is revealed in Fig. 4.2f. This means that they are connected three dimensionally. The growth morphology of the C grain indicated by the smaller black circle in the upper center is interesting because its entrance was narrow but grew wide. This type of growth is also observed at the growth front of the C grain indicated by the black circle in Fig. 4.2f.

After the three grains A, B and C impinged one another in Fig. 4.2f, there was no remarkable change in Fig. 4.2g. Comparing Fig. 4.2a with Fig. 4.2g, most matrix grains in Fig. 4.2a shrank away and disappeared in Fig. 4.2g. The disappearance of matrix grains was caused either by the growth of Goss grains or by the impingement of Goss grains, resulting in trapped matrix grains. Although Fig. 4.2 shows that matrix grains were trapped by the impingement of Goss grains, they can also be trapped inside one abnormally-growing Goss grain as shown in Fig. 4.3.

Fig. 4.3a is the IPF-ND map of the initial microstructure, which was heated at 1080℃ for 0 min and then cooled. After 6 min at 1080℃ Fig. 4.3a changed to Fig. 4.3b. After another 5 min, it

changed to Fig. 4.3c and after another 2.5 min it changed to Fig. 4.3d. The noticeable change is indicated by the black circle, where matrix grains were trapped inside the Goss grain. Most of the isolated grains disappeared in Fig. 4.3e, where the red and yellow grains in contact indicated by the black circle did not disappear but remained even after another 2 min at 1080°C as shown in Fig. 4.3f.

Then, how island grains are formed in an abnormally−growing Goss grain? There are two possibilities for the formation of island grains. One is the low mobility of their grain boundaries. This means that they are left behind the abnormally−growing Goss grain because their grain boundaries are immobile. The other possibility is that they are formed by SSW of the Goss grain. Using 3− dimensional MC simulations, Park et al. [36, 37] and Na et al. [41] showed how island grains are formed by sub−boundary enhanced SSW of an abnormally−growing grain. Especially, Na et al. [41] showed that the growth by sub−boundary enhanced SSW produced a highly irregular grain shape because the growth front with a high wetting probability makes a protrusion. When such protrusions meet each other, the matrix grains would be trapped two dimensionally by protrusions. In this case, these trapped grains appear to be island grains on some two dimensional sections. Likewise, the matrix grains can be trapped three dimensionally by protrusions.

Depending on how island grains are formed, the mechanism of AGG becomes quite different. Figs. 4.2 and 4.3 show that once trapped, island grains shrank very fast, indicating that their grain boundaries

are mobile rather than being immobile. Therefore, island grains should be formed by SSW.

Then, why island grains do shrink much faster than other matrix grains? This would be because island grains are free from the triple junction constraint, which other matrix grains have. In other words, an island grain generally shrinks in an accelerated way because its local curvature of grain boundary becomes larger as it shrinks. This means that depending on the presence and absence of the triple junction constraint, the growth kinetics changes drastically. If SSW occurs along the triple junction at the growth front, the Goss grain would be free from the triple junction constraint and could grow drastically fast.

Some of island grains did not disappear and tended to remain as indicated by the black circle in Fig. 4.3e and 4.3f or by the red circle in Fig. 4.3a－4.3f. It should be noted that the grain in the red circle in Fig. 4.3a－4.3f is difficult to identify because the color of the grain is hardly distinguishable from that of the surrounding Goss grain.

The misorientation of the grain in the red circle turns out to be 11.4°, which is a low angle. On the other hand, misorientations of the red and yellow grains in the black circle in Fig. 4.3e and 4.3f are respectively 53.8° and 40° with the surrounding Goss grain. Although the red and yellow grains have a high angle misorientation, the yellow grain and surrounding Goss grain have $\Sigma 7$ relationship. Therefore, they did not disappear but remained. Definitely it can be

said that disappearing grains have a higher mobility than remaining grains.

It should be noted that some island or peninsular grains indicated by the black circles did not disappear but remained from Fig. 4.2a to 4.2g. This means that these grains must have a relatively low mobility grain boundary with respect to the surrounding Goss grain. Measurements of misorientation angles between these grains and the surrounding Goss grain provide a very important information as to which grains have the low or high mobility boundary with the Goss grain.

Fig. 4.4 shows the time evolution as to how the Goss grain grew. To distinguish the abnormally−growing Goss grain from other grains, only the Goss grain is colored green and other grains are shown in a gray scale by the average image quality. Fig. 4.4a is the initial microstructure after heat treatment at 1080℃ for 0 min. At the lower right of Fig. 4.4a, there are one Goss grain. After 3 min heat treatment at 1080℃ in Fig. 4.4b, this Goss grain grew extensively as shown in Fig. 4.4b. Another very large Goss grain grew from the bottom right of Fig. 4.4b. The two large grains in Fig. 4.4b appear to be connected three dimensionally, which means they are an identical grain, because they became one after another 3 min as shown in Fig. 4.4c.

In Fig. 4.4b, large peninsular grains were formed as indicated by the circle. From the viewpoint of the mechanism that AGG occurs by high mobility boundaries, the formation of such large peninsular

grains may be attributed to the low mobility of their grain boundaries. This means that they are left behind the abnormally−growing Goss grain because their grain boundaries are immobile. However, most of peninsula grains disappeared after 3 min heat treatment in Fig. 4.4c, indicating that their grain boundaries are highly mobile. Therefore, the formation of peninsular grains should not be attributed to low mobility boundaries but be attributed to SSW.

The Goss grain in Fig. 4.4a grew as large as ~ 2000 μm in the vertical direction after 9 min as shown in Fig. 4.4d. This corresponds to the growth rate higher than ~ 200 μm/min. This growth rate is based on the time evolution obtained by the sequential heat treatment. If the heat treatment was continued for 9 min, the growth rate is expected to be even higher. Fig. 4.4d shows that the abnormally−growing Goss grain left island grains in the upper part behind, implying that the fast growth of the Goss grain is attributed to SSW.
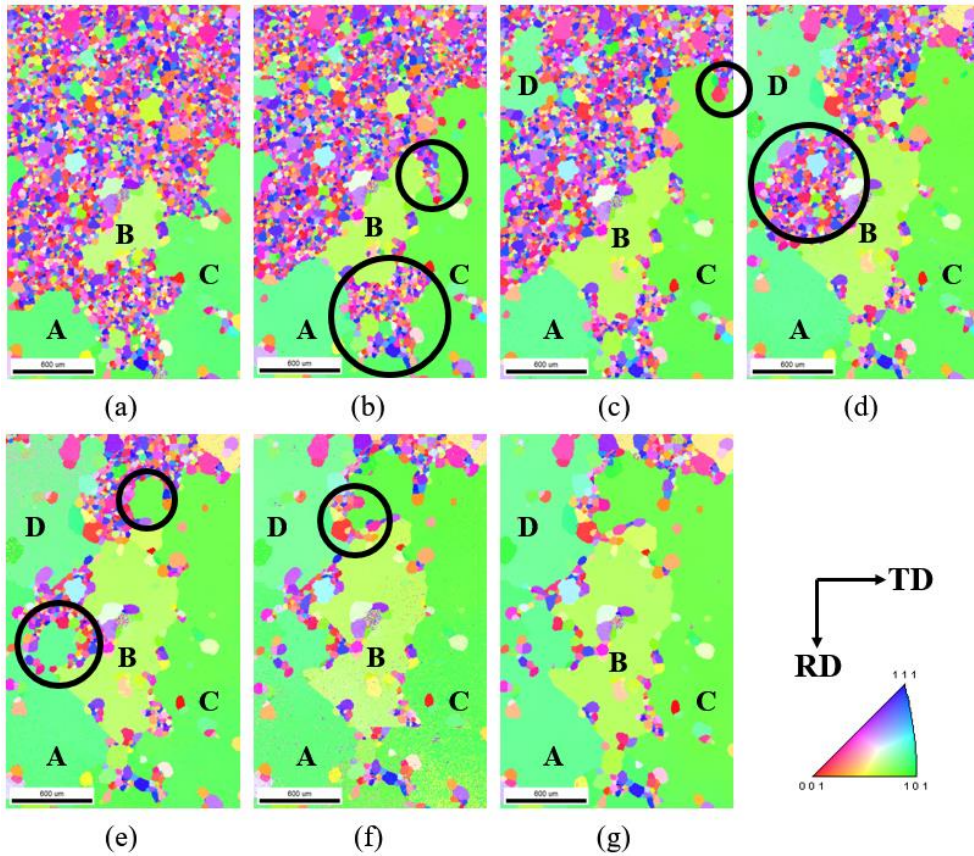
Fig. 4.2. EBSD IPF maps with time evolution of Goss grains during AGG. (a) The initial IPF map of the specimen heated to 1080℃ at 5℃/min, held for 0 min and cooled. IPF maps from (b) to (g) were obtained after annealing at 1080℃ sequentially for accumulated times of 5, 10, 15, 20, 25 and 30 min, respectively.
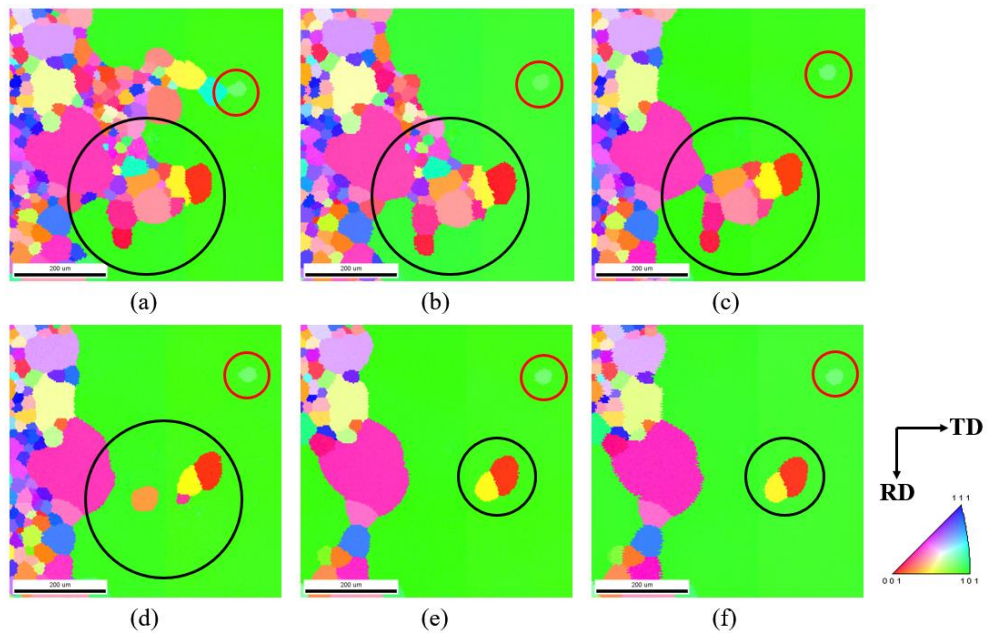
Fig. 4.3. High magnification EBSD IPF maps with time evolution of Goss grains during AGG. (a) The initial IPF map of the specimen heated to 1080°C at 5°C/min, held for 0 min and cooled. IPF maps from (b) to (f) were obtained after annealing at 1080°C sequentially for accumulated times of 6, 11, 13.5, 16 and 18 min, respectively.
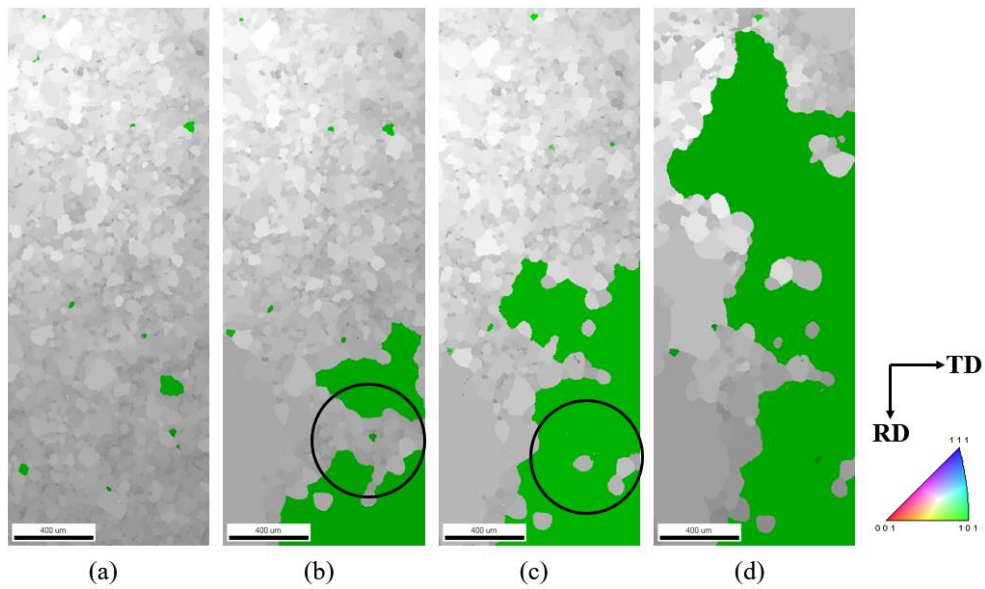
Fig. 4.4. EBSD IPF maps with time evolution of Goss grains during AGG. (a) The initial state IPF map of the specimen heated to 1080°C at 5°C/min, held for 0 min and cooled. IPF maps from (b) to (d) were obtained after annealing at 1080°C sequentially for accumulated times of 3, 6 and 9 min, respectively.

4.4 Conclusion

 The time sequential evolution of abnormally−growing Goss grains in Fe-3%Si steel was observed by EBSD. Numerous matrix grains were trapped by the impingement of abnormally−growing Goss grains. Besides, island and peninsular grains were formed by the highly irregular growth of Goss grains. Once matrix grains were trapped by the impingement or island and peninsular grains were formed, they tended to disappear much faster than before. This would be because these grains are free from the triple junction constraint, in which case the growth kinetics changes drastically. This indicates that they were formed not by their low grain boundary mobility but by SSW.

Chapter. 5 Misorientation characteristics at the growth front of abnormally-growing Goss grains in Fe-3%Si steel

5.1 Introduction

It is relatively easy to observe the penetrating morphologies at the growth front of abnormally−growing Goss grains in Fe−3%Si steel. In the mechanism of sub−boundary enhanced SSW [29−32, 37, 41, 53−55], it is highly probable that these penetrating morphologies would undergo SSW along the triple junction line.

Fig. 5.1a shows a 3−dimensional morphology of the triple junction wetting, which indicates that grain D grows by wetting along the triple junction line made by grains A, B, and C. Fig. 5.1b shows the 2−dimensional section in horizontal direction of the wetting. Therefore, if the penetrating morphology like Fig. 5.1b is observed on the polished surface of the specimen, it is highly likely that the penetrating grain undergoes SSW along the triple junction line. Fig. 5.1c shows the 2−dimensional section in vertical direction of the wetting. Notably, the 3−sided grain in Fig. 5.1c has a negative curvature. In the case where the grain boundary energy is isotropic, the 3−sided grain has a positive curvature and shrinks because the boundary migration occurs in the direction where the curvature disappears. The negative curvature in Fig. 5.1c indicates that the

3-sided grain does not shrink but rather grows. Therefore, if the 3-sided grain with a negative curvature like Fig. 5.1c is observed on the polished surface of the specimen, it is highly likely that the 3-sided grain undergoes SSW along the triple junction line.

The energetic condition for SSW of the grain D along the triple junction line made by grains A, B, and C is as follows, [62]

$$\gamma_{BC} + \gamma_{CD} + \gamma_{BD} > \sqrt{3}(\gamma_{AB} + \gamma_{AC} + \gamma_{AD}), \tag{5.1}$$

where γ represents the grain boundary energy, and the subscript represents the boundary of the two grains. Especially when grains A and D have sub-boundaries of a very low angle, their grain boundary energy would be very low. For example, the sub-boundaries experimentally observed in abnormally-growing Goss grains have 0.15° and 0.17° [33] and those in abnormally-growing grains in the aluminum 5052 alloy have 0.22° and 0.29° [35]. Considering that sub-boundaries have such small angles and as a result small energies, the energy of the sub-boundary between grains A and D can be approximated as zero. Then, it can be further approximated as

$$\gamma_{AB} \approx \gamma_{BD}, \gamma_{AC} \approx \gamma_{CD}. \tag{5.2}$$

If these approximations are applied to Eq. (5.1), the wetting condition of Eq. (5.1) can be simplified as

$$\gamma_{BC} > (\sqrt{3} - 1)(\gamma_{AB} + \gamma_{AC}). \tag{5.3}$$

According to Eq. (5.3), the triple junction wetting occurs if the grain boundary energy γ_{BC} is larger than 0.732 times of the sum of

γ_{AB} and γ_{AC}. Thus, the probability of growth by wetting increases substantially if the grain has sub-boundaries. These grains would grow exclusively faster, resulting in AGG.

According to Eq. (5.3), the penetrated boundaries should tend to have a high energy and the penetrating boundaries should tend to have a low energy. The purpose of this paper is to examine such possibility. The distribution of misorientation angles of 102 penetrated boundaries and 204 penetrating boundaries was examined using EBSD at the growth front of abnormally-growing Goss grains in Fe-3%Si steel. Furthermore, by converting the grain boundary energy from the misorientation angles, the possibility for the boundary energies of penetrating Goss and penetrated grains to satisfy Eq. (5.3) was also examined.
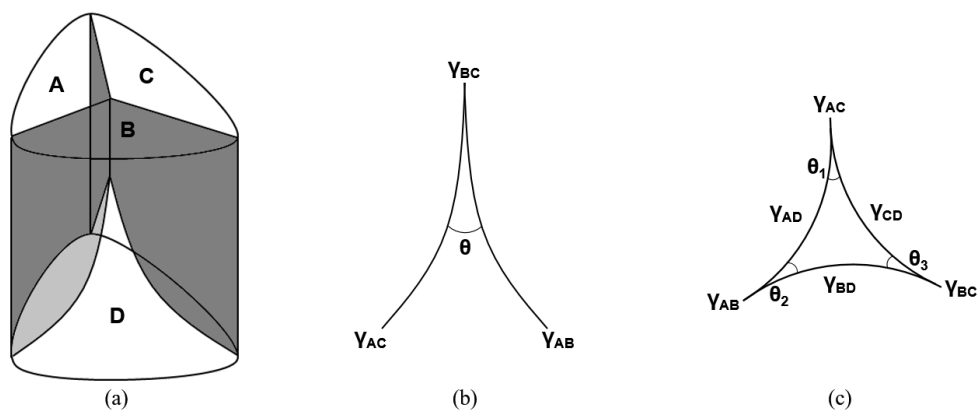
Fig. 5.1. (a) Schematic representation of triple-junction wetting morphology in 3-dimension. (b) and (c) are 2-dimensional section of wetting direction.

5.2 Experiment procedure

The Fe-3%Si steel ingot was hot-rolled to 2.3 mm and cold-rolled to 0.3 mm. Then, it was recrystallized for 150 sec at 850°C for decarburization and nitriding. The secondary recrystallization was carried out in the tube furnace under flowing hydrogen (99.9999%) to prevent the specimens from being oxidized. To observe the initial microstructure of secondary recrystallization, the specimen was heated at 5°C/min, held for 0 sec at 1080°C and cooled to room temperature. This specimen was polished to observe the microstructure and to analyze the misorientation by EBSD (EDAX, Hikari). Considering the grain size, the step size of the EBSD was 3.5 μm.

If AGG of Goss grains occurs by SSW along the triple junction, the penetrating morphology, which will be elaborated in detail in Figs. 5.2 and 5.5, would be observed at the growth front of abnormally-growing Goss grains. In order to confirm whether abnormally-growing Goss grains should penetrate into the grain boundary at the growth front, the specimens were further heated for 3 min at 1080°C and cooled to room temperature after the initial microstructure of secondary recrystallization was observed. After the treatment, the same region of interest from the initial microstructure of secondary recrystallization was observed and analyzed again by EBSD. The misorientation angle and CSL boundaries of grains were also analyzed by the software (OIM analysis, EDAX) to check if the penetrating Goss grains satisfy the

wetting condition along the triple junction of matrix grains at the growth front. The Σ values were determined using Brandon's criteria [58]. Then, the misorientation angle between penetrating and penetrated grains measured by EBSD can be converted to a grain boundary energy using the Read-Shockley functions as shown Eq. (3.1).

5.3 Results and discussion

Fig. 5.2 is the EBSD IPF map showing that a Goss grain penetrates into the boundary of grains A and B at the growth front. The misorientation between the two penetrated grains A and B is 36.4°. The misorientations between the penetrating Goss and the penetrated A grains and between the penetrating Goss and the penetrated B grains are 22.6° and 39.9°, respectively. If these misorientations are converted to the grain boundary energies using Eq. (3.1), it can be checked whether the penetrating morphology in Fig. 5.2 satisfies the wetting condition of Eq. (5.3).

We investigated dozens of abnormally−growing Goss grains having a penetrating morphology like Fig. 5.2 for statistical examination of the misorientation angles between the penetrated grains and between the Goss and the penetrated grains. A total of 102 abnormally−growing Goss grains were observed and analyzed, from which the distribution of misorientation angles between the penetrated boundaries was determined as shown in Fig. 5.3. Fig. 5.3a and 5.3b show the misorientation angle distribution and Σ values between the penetrated grains, respectively. It is notable that none of the penetrated boundaries has a misorientation angle less than 15° in Fig. 5.3a. Since there is no low misorientation angle in the penetrated boundaries, it is highly probable that their grain boundary energy should be high. Fig. 5.3b shows the absence of $\Sigma3$, $\Sigma5$ and $\Sigma9$, which are well−known CSL boundaries. Other CSL boundaries such as $\Sigma7$, $\Sigma13$ and $\Sigma21 \sim \Sigma49$ exist. However,

their percentage is only 5.9% of the 102 penetrated grain boundaries.

In contrast, penetrating boundaries, which are the boundaries between penetrating Goss and penetrated grains, exhibit a different distribution of misorientation angles. Fig. 5.4a and 5.4b show the misorientation angle distribution and Σ values of penetrating boundaries, respectively. It shows that the penetrating boundaries had a relatively high percentage of low angle misorientations less than 15°. 17.2% of the 204 penetrating Goss and penetrated matrix grains have low misorientation angles. Besides, the percentage of the CSL boundaries is also high: 23.5% of the 204 penetrating Goss and penetrated matrix grains have CSL boundaries. The aspect of Fig. 5.3 and 5.4 coincides with the misorientation angle measurements of penetrating morphologies at the growth front of abnormally−growing grains in Fe−3%Si steel reported by Park et al. [55] and in the aluminum alloy by Park et al. [62].

Considering this feature of misorientation angle distributions, in which the low angle misorientation is absent in the penetrated boundaries but exists in a relatively high percentage in the penetrating boundaries and the percentage of the CSL boundaries is low in the penetrated boundaries but relatively high in the penetrating boundaries, it is highly probable that the penetrating morphology of the abnormally−growing Goss grains in Fig. 5.2 satisfies the wetting condition of Eq. (5.3). This means that the penetrating morphologies in Fig. 5.2 represent the 2−dimensional

section of the wetting along the triple junction line, which is illustrated in Fig. 5.1b.

To further confirm that SSW took place, the growth front of the abnormally-growing Goss grains such as shown in Fig. 5.2 was traced after additional 3 min of heating at 1080°C. The growth front and island grains were compared before and after 3 min of heating. The resulting morphologies are shown in Fig. 5.5. Fig. 5.5a and 5.5c show the initial morphologies of the growth front and island grains, respectively. Fig. 5.5b and 5.5d are the morphologies after 3 min heat treatment of Fig. 5.5a and 5.5c, respectively.

At Fig. 5.5a and 5.5b, the red grain (number 2) disappears after the heating. As a result, the curvature of the Goss grain boundary shared with the yellow grain (number 1) increased. The curvature of the boundary between the Goss and the yellow grains increased as a result of the disappearance of the red grain in Fig. 5.5b.

Fig. 5.5c shows three island grains inside the abnormally-growing Goss grain. Fig. 5.5d shows that the blue grain (number 4) disappears after 3 min of heating. If SSW drives the migration of the Goss grain boundaries in Fig. 5.5a and 5.5c, the related grain boundary energy would satisfy the energetic conditions of Eq. (5.3).

To check such possibility, the three misorientation angles between the grain 1 and 2, between the Goss and the grain 2 and between the Goss and the grain 1 were measured and converted into the grain boundary energies. The misorientation angle between the grains 1 and 2 in Fig. 5.5a is $31.8^{\circ}/[-3\ -5\ -6]$, which is converted

to the grain boundary energy of 1.28 J/m^2 based on the report by Kim et al. [57] and Read—Shockley function [56]. In the same manner, the misorientation angle between the Goss grain and the grain 2 is 49.1°/[11 6 2], which corresponds to the grain boundary energy of 1.25 J/m^2. Finally, the misorientation between the Goss grain and the grain 1 is 56.1°/[−10 8 −11], which is Σ3 under the Brandon criterion [58]. It has the relatively low grain boundary energy of 0.49 J/m^2 and is consistent with other reports from Ratanaphan et. al. [63] and Tschopp et. al. [64] that Σ3 relationship generally has low energy. From the energies determined, it was confirmed whether these grain boundary energies satisfy the wetting condition of Eq. (5.3). If the energies of 1.28, 1.25 and 0.49 are substituted into Eq. (5.3), 1.28 J/m^2 > ($\sqrt{3}$−1)(0.49 + 1.25) = 1.27 J/m^2, the result of which satisfies Eq. (5.3).

Furthermore, the misorientation between the grains 3 and 4 in Fig. 5.5c is 44.3°/[2 −1 −3], which is converted to 1.31 J/m^2 and that between the Goss and the grain 4 is 30.3°/[0 −7 −2], which is converted to 1.22 J/m^2. Finally, the misorientation angle that between the Goss and the grain 3 is 59.9°/[−7 −7 −6], which is Σ3. The energy is 0.41 J/m^2. If these energies are substituted into Eq. (5.3), 1.31 J/m^2 > ($\sqrt{3}$−1)(0.41 + 1.22) = 1.19 J/m^2, the result of which satisfies Eq. (5.3).

Fig. 5.5a and 5.5c have the same Σ3 relationship but their grain boundary energies are different. It is because they have different

deviation angles. The deviation angle between the Goss grain and the grain 1 in Fig. 5.5a is 7.1°, and the deviation angle between the Goss grain and the grain 3 in Fig. 5.5c is 4.1°. The difference of the deviation angle results in difference of grain boundary energies in accordance with Read–Shockley function [56].

Meanwhile, the absence of a low angle grain boundary in the penetrated grain boundaries in Fig. 5.3 and the relative high frequency of low angle and CSL boundaries in the penetrating grain boundaries in Fig. 5.4 strongly indicate that the Goss grains in Figs. 5.2 and 5.5 grow by SSW. Furthermore, considering that the grain boundary migration of the Goss grain is accompanied with increasing grain boundary curvature at the growth front as shown in Fig. 5.5 and that the grain boundary energies satisfy Eq. (5.3), it is highly probable that the SSW mechanism is applicable to AGG phenomenon.
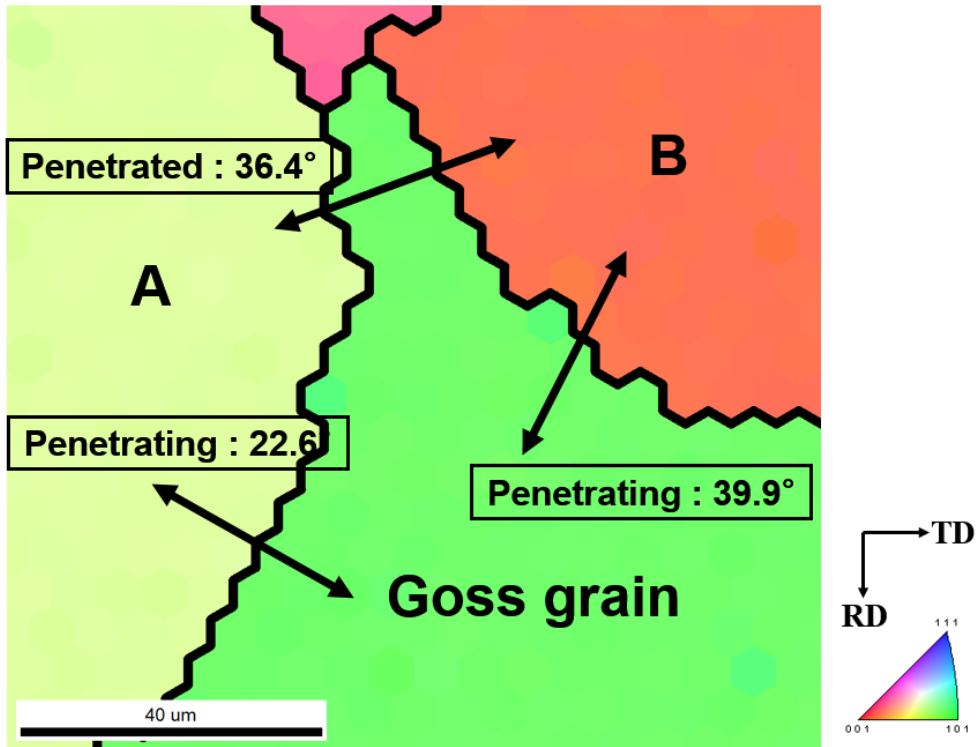
Fig. 5.2. EBSD IPF map of penetrating morphology at the growth front of Goss grain. The specimen heated up at 1080°C for 5°C/min, held 0 sec.
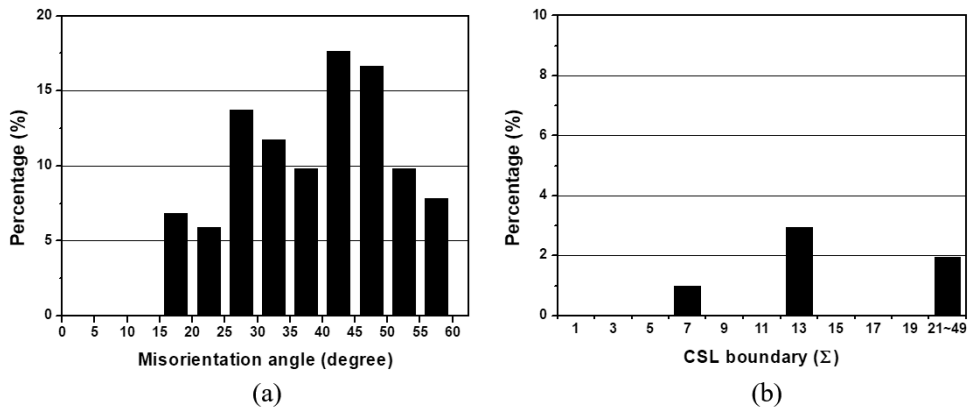
Fig. 5.3. (a) Misorientation angle distribution and (b) percentage of low angle and CSL boundaries in 102 penetrated grain boundaries.
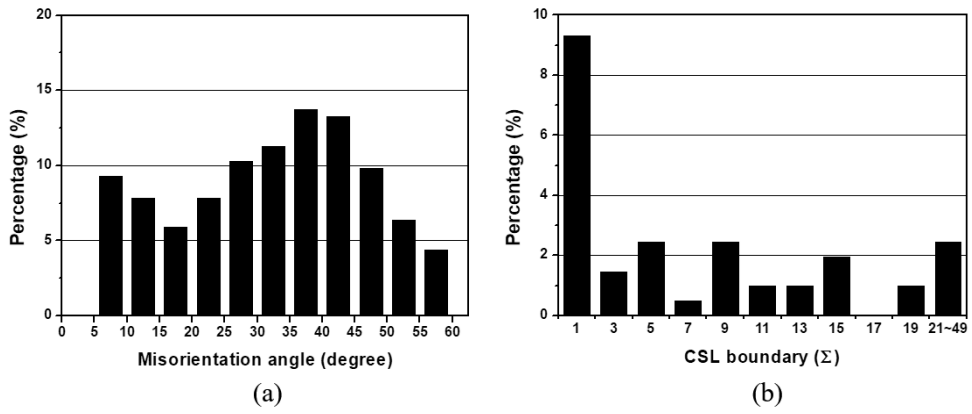
Fig. 5.4. (a) Misorientation angle distribution and (b) percentage of low angle and CSL boundaries in 204 penetrating grain boundaries.
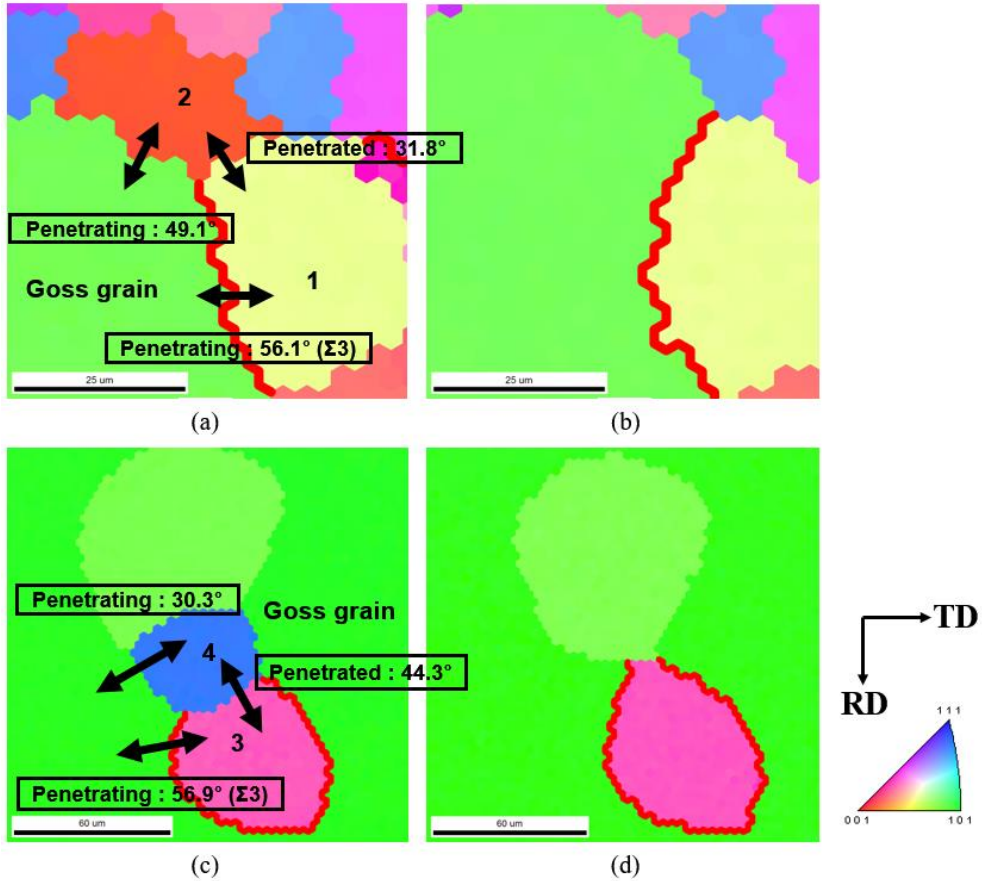
Fig. 5.5. EBSD IPF maps of penetrating morphology at the growth front of Goss grain. (a) and (c) are the IPF map after heated at 1080℃ for 5℃/min, held 0 sec, (b) and (d) are the IPF map of the same area as (a) and (c) after additional heat treatment for 3 min.

5.4 Conclusion

In the distribution of misorientation angles in the 102 penetrated grains at the growth front of abnormally−growing Goss grains, there is no low angle grain boundary. However, 17.2% and 23.5% of the 204 penetrating grain boundaries have low misorientation angles and CSL boundaries, respectively. These results strongly suggest that Goss grains grow by SSW. Moreover, the grain boundary energies estimated from the misorientation angle satisfy the wetting condition of Eq. (5.3). These results support the SSW mechanism for the AGG in Fe−3%Si steel.

Chapter. 6 Conclusion

In order to check role of sub-boundaries at AGG, non-Goss grains was induced by applying local deformation using indentation in Fe-3%Si steel. All abnormally-growing grains had sub-boundaries inside them with very low misorientation angle below 0.6°, whereas other matrix grains did not have sub-boundaries without exception.

Also, the Goss grains undergo to AGG and these several Goss grains were analyzed using synchrotron XMD to measure sub-boundary angles. As with the previous results, all abnormally-growing Goss grains had sub-boundaries with misorientations less than 1° and all matrix grains examined had no sub-boundaries. Also, small Goss grains tended to have large sub-boundary angles and vice versa.

Meanwhile, the time sequential evolution of abnormally-growing Goss grains in Fe-3%Si steel was observed by EBSD. The island and the peninsular grains were formed by the highly irregular growth of Goss grains. Once matrix grains were trapped by the impingement or island and peninsular grains were formed, they tended to disappear much faster than before.

Finally, the distribution of misorientation angles in the 102 penetrated grains at the growth front of abnormally-growing Goss grains, there is no low angle grain boundary. However, 17.2% and 23.5% of the 204 penetrating grain boundaries have low misorientation angles and CSL boundaries, respectively. Moreover, the grain boundary energies estimated from the misorientation

angle satisfy the wetting condition of Eq. (5.3). These results support the SSW mechanism for the AGG in Fe－3%Si steel.

Reference

[1] R. Messina, M. Soucail, T. Baudin, L.P. Kubin, Observations of and model for insular grains and grain clusters formed during anomalous grain growth in N18 superalloy, J. Appl. Phys. 84 (1998) 6366-6371.

[2] S.H. Lee, J.S. Choi, D.Y. Yoon, The dependence of abnormal grain growth on initial grain size in 316 L stainless steel, Z. Met. 92 (2001) 655-662.

[3] B. Sarrail, C. Schrupp, S. Babakhanyan, K. Muscare, J. Foyos, J. Ogren, S. Sparkowich, R. Sutherlin, J. Hilty, R. Clark Jr, O.S. Es-Said, Annealing and anomalous (bimodal) grain growth of Zr 702, Eng. Failure Anal. 14 (2007) 652-655.

[4] H.C. Kim, C.G. Kang, M.Y. Huh, O. Engler, Effect of primary recrystallization texture on abnormal grain growth in an aluminum alloy, Scr. Mater. 57 (2007) 325-327.

[5] T. Omori, T. Kusama, S. Kawata, I. Ohnuma, Y. Sutou, Y. Araki, K. Ishida, R. Kainuma, Abnormal grain growth induced by cyclic heat treatment, Science 341 (2013) 1500-1502.

[6] M. Shirdel, H. Mirzadeh, M.H. Parsa, Abnormal grain growth in AISI 304L stainless steel, Mater. Charact. 97 (2014) 11-17.

[7] J.S. Choi, D.Y. Yoon, The temperature dependence of abnormal grain growth and grain boundary faceting in 316L stainless steel, ISIJ Int. 41 (2001) 478-483.

[8] Y.B. Chun, S.K. Hwang, S.I. Kwun, M.H. Kim, Abnormal grain growth of Zr-1wt.%Nb alloy and the effect of Mo addition, Scr. Mater. 40 (1999) 1165-1170.

[9] J. Dennis, P.S. Bate, F.J. Humphreys, Abnormal grain growth in Al-3.5Cu, Acta Mater. 57 (2009) 4539-4547.

[10] U. Klement, M. da Silva, Individual grain orientations and texture development of nanocrystalline electrodeposits showing abnormal grain growth, Journal of Alloys and Compounds 434-435 (2007) 714-717.

[11] F.J. Humphreys, M. Hatherly, Recrystallization and related annealing phenomena, 1st ed., Pergamon Press, Oxford, 1995.

[12] N.P. Goss, New development in electrical strip steels characterized by fine grain structure approaching the properties of a single crystal, Trans. Am. Soc. Met. 23 (1935) 511-531.

[13] J. Harase, R. Shimizu, Texture evolution by grain growth in the presence of MnS and AIN precipitates in Fe-3% Si alloy, Acta Metall. Mater. 38 (1990) 1395-1403.

[14] J. Harase, R. Shimizu, Mechanism of secondary recyrstallization in grain oriented silicon steel, J. Jpn. I. Met. 54 (1990) 1-8.

[15] J. Harase, R. Shimizu, D.J. Dingley, Texture evolution in the presence of precipitates in Fe-3% Si alloy, Acta Metall. Mater. 39 (1991) 763-770.

[16] J. Harase, R. Shimizu, J.K. Kim, J.S. Woo, The role of high energy boundaries and coincidence boundaries in the secondary recrystallization of grain-oriented silicon steel, Met. Mater. Int. 5 (1999) 429-435.

[17] Y. Hayakawa, M. Muraki, J.A. Szpunar, The changes of grain boundary character distribution during the secondary recrystallization of electrical steel, Acta Mater. 46 (1998) 1063-1073.

[18] Y. Hayakawa, J.A. Szpunar, A new model of Goss texture development during secondary recrystallization of electrical steel, Acta Mater. 45 (1997) 4713-4720.

[19] N. Rajmohan, J.A. Szpunar, An analytical method for characterizing grain boundaries around growing Goss grains during secondary recrystallization, Scr. Mater. 44 (2001) 2387-2392.

[20] N. Rajmohan, J.A. Szpunar, Y. Hayakawa, A role of fractions of mobile grain boundaries in secondary recrystallization of Fe-Si steels, Acta Mater. 47 (1999) 2999-3008.

[21] A.L. Etter, T. Baudin, R. Penelle, Influence of the Goss grain neighbourhood during secondary recrystallization of Fe-3%Si

sheets, Mater. Sci. Forum, 2002, pp. 1251-1256.

[22] A.L. Etter, T. Baudin, R. Penelle, Influence of the Goss grain environment during secondary recrystallisation of conventional grain oriented Fe-3%Si steels, Scr. Mater. 47 (2002) 725-730.

[23] A. Morawiec, Grain misorientations in theories of abnormal grain growth in silicon steel, Scr. Mater. 43 (2000) 275-278.

[24] Y. Ushigami, T. Kumano, T. Haratani, S. Nakamura, S. Takebayashi, T. Kubota, Secondary recrystallization in grain-oriented silicon steel, 467-470 (2004) 853-862.

[25] Y. Ushigami, S. Nakamura, Mechanism of secondary recrystallization in grain-oriented Si steel, Mater. Sci. Forum, 2012, pp. 122-127.

[26] Y. Ushigami, S. Nakamura, S. Takebayashi, S. Suzuki, Effect of grain boundary character on selective growth of Goss grain in Fe-3%Si alloy, Mater. Sci. Forum, 2002, pp. 973-978.

[27] H. Homma, B. Hutchinson, Orientation dependence of secondary recrystallisation in silicon-iron, Acta Mater. 51 (2003) 3795-3805.

[28] H. Homma, K. Murakami, T. Tamaki, N. Shibata, T. Yamamoto, Y. Ikuhara, Effects of grain boundary characters for secondary recrystallisation in grain oriented silicon steel, Mater. Sci. Forum 558-559 (2007) 633-640.

[29] N.M. Hwang, New understanding of abnormal grain growth approached by solid-state wetting along grain boundary or triple junction, in: B. Bacroix, J.H. Driver, R. Gall, C. Maurice, R. Penelle, H. Regle, L. Tabourot (Eds.) Annecy, 2004, pp. 745-750.

[30] N.M. Hwang, S.B. Lee, D.Y. Kim, Abnormal grain growth by solid-state wetting along grain boundary or triple junction, Scr. Mater. 44 (2001) 1153-1160.

[31] S.B. Lee, N.M. Hwang, C.H. Han, D.Y. Yoon, Formation of islands and peninsulas of fine grains during the secondary recrystallization of an Fe-3wt% Si steel, Scr. Mater. 39 (1998) 825-829.

[32] H.S. Shim, N.M. Hwang, Secondary recrystallization in metals: approach by solid-state wetting, Korean J. Met. Mater. 52 (2014) 663-687.

[33] H.K. Park, S.D. Kim, S.C. Park, J.T. Park, N.M. Hwang, Sub-boundaries in abnormally growing Goss grains in Fe-3% Si steel, Scr. Mater. 62 (2010) 376-378.

[34] H.-S. Shim, T.-W. Na, J.-S. Chung, S.-B. Kwon, K. Gil, J.-T. Park, N.-M. Hwang, Synchrotron X-ray microdiffraction of Fe-3 wt%Si steel focusing on sub-boundaries within Goss grains, Scr. Mater. 116 (2016) 71-75.

[35] H.K. Park, H.G. Kang, C.S. Park, M.Y. Huh, N.M. Hwang, Ex situ observation of microstructure evolution during abnormal grain growth in aluminum alloy, Metall. Mater. Trans. A 43 (2012) 5218-5223.

[36] C.S. Park, T.W. Na, J.K. Kang, B.J. Lee, C.H. Han, N.M. Hwang, Parallel three-dimensional Monte Carlo simulations for effects of precipitates and sub-boundaries on abnormal grain growth of Goss grains in Fe-3%Si steel, Phil. Mag. 93 (2013) 4198-4212.

[37] C.S. Park, T.W. Na, H.K. Park, B.J. Lee, C.H. Han, N.M. Hwang, Three-dimensional Monte Carlo simulation for the effect of precipitates and sub-boundaries on abnormal grain growth, Scr. Mater. 66 (2012) 398-401.

[38] D.K. Lee, K.J. Ko, B.J. Lee, N.M. Hwang, Monte Carlo simulations of abnormal grain growth by sub-boundary-enhanced solid-state wetting, Scr. Mater. 58 (2008) 683-686.

[39] H.K. Park, S.J. Kim, H. Nam Han, C.H. Han, N.M. Hwang, Deformation feature of Goss grains in Fe-3% Si steel focused on stored energy after cold rolling, Mater. Trans. 51 (2010) 1547-1552.

[40] C. Braun, J.M. Dake, C.E. Krill, R. Birringer, Abnormal grain growth mediated by fractal boundary migration at the nanoscale, Sci. Rep. 8 (2018) 1592.

[41] T.-W. Na, D.-H. Cho, C.-S. Park, J.-T. Park, H.N. Han, N.-M. Hwang, Comparison of three-dimensional morphologies of

abnormally growing grains between Monte Carlo simulations and experiments of Fe−3% Si steel, Mater. Charact. 144 (2018) 239−246.

[42] T.−Y. Kim, H.−S. Shim, S. Kim, S. Choi, T.−W. Na, D. Kwon, N.−M. Hwang, Synchrotron X−ray microdiffraction analysis of abnormally growing grains induced by indentation in Fe−3% Si steel, Mater. Charact. 156 (2019) 109845.

[43] V. Randle, O. Engler, Introduction to texture analysis: macrotexture, microtexture and orientation mapping, 1st ed., CRC press, London, 2000.

[44] A.S. Budiman, W.D. Nix, N. Tamura, B.C. Valek, K. Gadre, J. Maiz, R. Spolenak, J.R. Patel, Crystal plasticity in Cu damascene interconnect lines undergoing electromigration as revealed by synchrotron X−ray microdiffraction, Appl. Phys. Lett. 88 (2006) 233−515.

[45] N. Tamura, A.A. MacDowell, R. Spolenak, B.C. Valek, J.C. Bravman, W.L. Brown, R.S. Celestre, H.A. Padmore, B.W. Batterman, J.R. Patel, Scanning X−ray microdiffraction with submicrometer white beam for strain/stress and orientation mapping in thin films, J. Synchrotron Radiat. 10 (2003) 137−143.

[46] A. Budiman, Synchrotron white−beam X−ray microdiffraction at the advanced light source, Berkeley Lab, in: Springer (Ed.), Probing crystal plasticity at the nanoscales: synchrotron X−ray microdiffraction, Springer, Singapore, 2015, pp. 15−35.

[47] G.E. Ice, R.I. Barabash, White beam microdiffraction and dislocations gradients, in: F.N.R. Nabarro, M.S. Duesbery (Eds.), Dislocations in solids, Elsevier, North−Holland, 2007, pp. 499−601.

[48] F. Citrawati, M.Z. Quadir, P.R. Munroe, Grain Boundary Deformation Phenomena and Secondary Growth of Goss Grains in a Fe−3.5%Si Steel, ISIJ Int. 57 (2017) 1874−1882.

[49] J.B. Koo, D.Y. Yoon, M.F. Henry, The effect of small deformation on abnormal grain growth in bulk Cu, Metall. Mater. Trans. A 33 (2002) 3803−3815.

[50] Y.K. Cho, D.Y. Yoon, M.F. Henry, The effects of deformation

and pre-heat-treatment on abnormal grain growth in RENÉ 88 superalloy, Metall. Mater. Trans. A 32 (2001) 3077-3090.

[51] D.K. Kim, Abnormal grain growth in Fe-3%Si steel induced by laser annealing and low deformation, Materials science and engineering, Seoul National University, Seoul, 2012.

[52] T.-W. Na, H.-K. Park, C.-S. Park, J.-T. Park, N.-M.J.A.M. Hwang, Misorientation angle analysis near the growth front of abnormally growing grains in 5052 aluminum alloy, Acta Mater. 115 (2016) 224-229.

[53] K.J. Ko, A.D. Rollett, N.M. Hwang, Abnormal grain growth of Goss grains in Fe-3% Si steel driven by sub-boundary-enhanced solid-state wetting: analysis by Monte Carlo simulation, Acta Mater. 58 (2010) 4414-4423.

[54] K.J. Ko, P.R. Cha, D. Srolovitz, N.M. Hwang, Abnormal grain growth induced by sub-boundary-enhanced solid-state wetting: Analysis by phase-field model simulations, Acta Mater. 57 (2009) 838-845.

[55] H. Park, D.Y. Kim, N.M. Hwang, Y.C. Joo, C.H. Han, J.K. Kim, Microstructural evidence of abnormal grain growth by solid-state wetting in Fe-3%Si steel, J. Appl. Phys. 95 (2004) 5515-5521.

[56] W.T. Read, W. Shockley, Dislocation models of crystal grain boundaries, Phys. Rev. 78 (1950) 275-289.

[57] H.-K. Kim, W.-S. Ko, H.-J. Lee, S.G. Kim, B.-J. Lee, An identification scheme of grain boundaries and construction of a grain boundary energy database, Scr. Mater. 64 (2011) 1152-1155.

[58] D. Brandon, The structure of high-angle grain boundaries, Acta Metall. 14 (1966) 1479-1484.

[59] B.-J. Lee, S.-H. Choi, Computation of grain boundary energies, Modelling Simul. Mater. Sci. Eng. 12 (2004) 621-632.

[60] M.P.Anderson, G.S.Grest, R.D.Doherty, K. Li, D.J. Srolovitz, Inhibition of grain growth by second phase particles: Three dimensional Monte Carlo computer simulations, Scr. Metall. 23 (1989) 753-758.

[61] D.J. Srolovitz, G.S. Grest, M.P. Anderson, Computer simulation of grain growth-V. Abnormal grain growth, Acta Metall. 33 (1985) 2233-2247.

[62] C.S. Park, T.W. Na, H.K. Park, D.K. Kim, C.H. Han, N.M. Hwang, Misorientation characteristics of penetrating morphologies at the growth front of abnormally growing grains in aluminum alloy, Phil. Mag. Lett. 92 (2012) 344-351.

[63] S. Ratanaphan, D.L. Olmsted, V.V. Bulatov, E.A. Holm, A.D. Rollett, G.S. Rohrer, Grain boundary energies in body-centered cubic metals, Acta Mater. 88 (2015) 346-354.

[64] M.A. Tschopp, K.N. Solanki, F. Gao, X. Sun, M.A. Khaleel, M.F. Horstemeyer, Probing grain boundary sink strength at the nanoscale: Energetics and length scales of vacancy and interstitial absorption by grain boundaries in α-Fe, Phys. Rev. B 85 (2012) 064108.

국문 초록

3% 규소강판 내 고스 입자의 비정상 입자 성장

특정 입자들이 다른 입자들에 보다 매우 크게 성장하는 비정상 입자 성장 또는 이차 재결정은 금속계에서 잘 알려져 있다. 이런 현상은 특히 {110}<001> 고스 방위를 가지는 입자들이 비정상 입자 성장을 겪어 강한 고스 집합조직을 가지게 되는 3% 규소 강판에서 연구되어왔다. 고스 입자의 선택적 비정상 입자 성장 기구는 1935년 Goss에 의해 처음 보고된 이후로 아직 명확하게 밝혀지지 않았다. 본 연구 그룹에서는 아결정립계가 젖음의 확률을 증가시켜 금속에서 비정상 입자 성장을 유도하는 아결정립계에 의한 고상 젖음 이론을 주장해왔다. 본 논문에서는 이 이론을 바탕으로 3% 규소강판 내의 고스 입자의 비정상 입자 성장을 연구했다.

우선, 3% 규소강판에서 경도 측정기를 이용한 압입이 고스 그레인이 아닌 그레인들의 비정상 입자 성장에 미치는 영향을 연구하였다. 일차 재결정된 시편에 다양한 무게로 압입하여 이용하여 국부적으로 변형을 주고 860도에서 10분간 재결정 및 회복 열처리를 하였다. 싱크로트론 X-선 미세회절 분석 결과, 모든 비정상 성장 입자들이 0.6도 이하의 아결정립계를 가지고 있고 다른 입자에서는 아결정립계가 발견되지 않았다.

그리고 고상 젖음 이론에 의하면, 젖음 확률은 아결정립계의 각도가 감소할수록 증가하기 때문에, 작은 아결정립계 각도는 더 큰 비성장 성장 입자를 만들 수 있을 것이다. 이 가능성을 시험하고자 아결정립계의 각도 크기가 비정상 입자 성장의 거동에 미치는 영향을 연구하였다. 그 결과 모든 비정상 성장한 모든 고스 입자들이 1도 미만의 이결정립계를 가지고 있었고, 다른 입자들은 아결정립계가 존재하지 않았다. 또한 작은 고스 입자들일수록 큰 아결정립계 각도를 가지고 있었고 그 반대도

성립하였다. 이 결과는 아결정립계 각도가 비정상 성장 입자들의 크기에 중요한 변수가 될 수 있다는 것을 의미한다.

한편, 기존엔 하지 못했던 후방 전자 산란 장비를 이용한 3% 규소강판 내 비정상 성장한 고스 입자들 변화를 시간 순차적으로 관찰하였다. 몇몇 입자들은 성장 전선에서 고립되어 섬 입자들을 생성하였고, 불규칙한 성장은 불완전한 종종 고립을 초래하여 반도 입자를 생성하였다. 수많은 입자들이 비정상성장하는 고스 입자에 의해 고립되었고, 일단 섬이나 반도 입자들이 고립되면 이전보다 훨씬 빨리 줄어들었다.

마지막으로 3% 규소강판 내 비정상 고스 입자들의 성장 전선에서의 침투 형태를 연구하였다. 102개의 침투 당한 입계와 204개의 침투한 비정상 성장 고스 입자들의 형태를 조사한 결과, 102개의 침투 당한 입계들에서는 15도 미만의 낮은 결정 방위 차이가 존재하지 않았다. 반면에 204개의 침투한 입계들 중 17.2%는 낮은 결정 방위 차이를 가지고 있었고, 일치 위치 격자들도 23.5%가 존재했다. 또한, 침투 형태에서 세 입자의 결정 방위 차이로부터 얻어진 고스 입자들의 입계 에너지는 삼중 접합선을 따라 고상 젖음 이론에 대한 에너지 조건을 만족하였다.

본 논문에서 실행된 모든 실험 결과들은 3% 규소강판 내 고스 입자들의 비정상 입자 성장이 아결정립계에 의한 고상 젖음 이론에 의해 발생하는 것을 의미한다.